Quantifying the variability in fault density across the UK Bowland Shale with implications for induced seismicity hazard

Germán Rodríguez-Pradilla , James P. Verdon [*,1]

School of Earth Sciences, University of Bristol, Wills Memorial Building, Queen's Road, BS8 1RJ Bristol, UK

A R T I C L E   I N F O

A B S T R A C T

To date, hydraulic fracturing for shale gas extraction has been used at three wells in the UK. In each case, the resulting microseismicity exceeded the UK's red-light threshold of magnitude 0.5. The three wells all targeted the Bowland Shale Formation, and all were located within close proximity of each other on the Fylde Peninsula in west Lancashire. Observations of hydraulic fracturing-induced seismicity (HF-IS) elsewhere shows that the prevalence of induced seismicity is highly spatially variable. Hence, it is by no means clear whether hydraulic fracturing elsewhere in the Bowland Shale would be likely to generate seismicity at similar levels. In this study we examine the geological and geomechanical conditions across the Bowland Shale with respect to their potential controls on induced seismicity. The abundance of pre-existing faults is likely to play an important control on the generation of HF-IS. We use an automated fault detection algorithm to map faults within a selection of 3D reflection seismic datasets across the Bowland Shale play. For the identified faults, we compute the effective stresses acting on these structures in order to identify whether they are likely to be critically stressed. We find that the Bowland Shale within the Fylde Peninsula contains a significant number of critically stressed faults. However, there is significant variation in the density of critically stressed faults across the play, with up to an order of magnitude reduction in fault density from the west (i.e., the Fylde Peninsula) to the east. We use these observations to inform a seismic hazard model for proposed hydraulic fracturing in areas to the east of the Bowland Shale play. We find that the occurrence of felt seismic events cannot be precluded, however their likelihood of occurring is reduced.

1. Introduction

Induced seismicity can be generated by any activity that perturbs the state of stress in the subsurface. In the UK, induced seismicity has been generated by geothermal stimulation[42,34], coal mining[9,68], and hydraulic fracturing[16,18,39] (HF hereafter). The induced seismicity generated in these cases has been of low magnitude ($M \leq 3.0$) but has generated significant levels of political and public interest[33,26].

The Bowland Shale, which is of Lower Carboniferous age, is thought to be the largest shale play in the UK with some resource estimates giving gas in place values of over 30 trillion cubic metres[2]. Fig. 1 shows the extent of the Bowland Shale play across northern England. In 2011 HF at the Preese Hall (PH hereafter) well generated an M_L 2.3 earthquake[16]. This event was felt by nearby residents. In response to this event the UK regulator (the Oil and Gas Authority, OGA, now renamed to the North Sea Transition Authority, NSTA) imposed a moratorium

before implementing a Traffic Light Scheme (TLS) to manage future cases of HF-induced seismicity (HF-IS).

In 2018 HF of the Preston New Road (PNR hereafter) 1z well produced six events that exceeded the M_L 0.5 red-light TLS threshold, which required the operator to pause operations for a minimum of eighteen hours in each case[18]. The largest event during stimulation of PNR-1z reached M_L 1.5. In 2019 the stimulation of the adjacent PNR-2 well generated an M_L 2.9 event that was felt in the nearby town of Blackpool. In response to this event, the regulator halted further operations, and a nationwide moratorium on HF for onshore shale gas was then imposed by the UK Government (note that this moratorium does not preclude hydraulic fracturing in conventional reservoirs, or any offshore oilfield activities). This moratorium was temporarily lifted by the brief Liz Truss government in 2022, but then re-imposed under Rishi Sunak's leadership. This to-and-fro highlights the highly politicised nature of shale gas development in the UK.

---

* Corresponding author.
  E-mail address: James.Verdon@bristol.ac.uk (J.P. Verdon).
[1] Orcid: 0000-0002-8410-2703

The prevalence of HF-IS is highly variable between and within geological formations[66], and can change significantly over relatively small distances. For example, in the Western Canada Sedimentary Basin (WCSB), activities in the Duvernay Shale have generated HF-IS in the Fox Creek[7] and Red Deer[57] areas, but HF-IS has been limited or non-existent across the rest of the play. Even within the Fox Creek area, the prevalence of HF-IS has varied substantially along a west-to-east axis over distances of a few 10 s of km[55,56,66]. Likewise, in the Appalachian Basin the occurrence of HF-IS from activities in the Utica Shale is found along a north-south trend along the eastern edge of Ohio[14], but has not occurred elsewhere, while HF-IS has been almost non-existent during operations in the overlying Marcellus Shale[59,66].

Given the observed spatial variability in the occurrence of HF-IS, and since the PH and PNR wells are located within 4 km of each other on the Fylde Peninsula in western Lancashire (Fig. 1b), it is therefore by no means a given that HF operations in the Bowland Shale in other regions of northern England will generate similar levels of induced seismicity.

Current research is shedding light on the factors that control the prevalence of HF-IS between and within shale plays. While no single factor can account for all the observed variability in HF-IS[66], key factors appear to include pore pressure gradients[23], stress conditions[51], and the abundance of pre-existing faulting, or proxies thereof[74].

In this study our objective is to examine the variability of these factors across the Bowland Shale, thereby assessing whether the levels of HF-IS observed during operations on the Fylde Peninsula might be expected across the entirety of the Bowland Shale play.

2. Regional fault density

Fig. 2a shows geological faults mapped across northern England within the study area defined by Andrews[2]. The fault maps have been produced by bedrock geological mapping at a scale of 1:50,000[4]. Fig. 2b maps the resulting fault density (total length of faulting per unit area) within 20 × 20 km blocks. We observe that the density of faulting is generally higher in the north and west of the study area, decreasing towards the south and east. This is consistent with the geological interpretation compiled by Andrews[2], where Figure 42 of that report shows a high density of faulting, with large offsets, within the Bowland, Blacon and Cheshire Basins, with the density of faulting decreasing substantially across the Nottingham Shelf and Gainsborough Trough.

However, while the mapping resolution for the data shown in Fig. 2 is consistent across the study area, the ability to identify and map faults will be determined by the quality of outcrop and exposure. As such, it is by no means certain that the apparent variations in fault density seen in Fig. 2 are actually representative of the density of faulting across the region. Moreover, this map shows faults that can be mapped at the surface, which implies faults that extend through whichever geological formations outcrop at the surface at the location in question. However, many faults may extend through the Carboniferous strata (i.e., the Bowland Shale) but not through the overlying Mesozoic rocks that represent the surface geology across much of this area – such structures would not be identified by geological bedrock mapping.

3. 3D seismic interpretation

3.1. Datasets

For a more detailed assessment of fault abundance we turn to 3D reflection seismic data. While 3D seismic coverage is patchy and does not provide coverage across the entire area of interest, these survey data offer the best opportunity of characterising faults within the Bowland Shale and identifying any variations in faulting across the study region. We identified and acquired post-stack seismic data cubes from the UK Onshore Geophysical Library (see Data and Resources) for six relatively modern-vintage 3D surveys across northern England (Fig. 2a). We accessed structural interpretations of key horizons and faults from operating companies and the BGS. Details of each survey are listed in Table 1, including the year of acquisition (and any re-processing), the survey area, the bin size for common-mid-point (CMP) gathers, the maximum fold, and details of any manual interpretations used in our analysis. The selected surveys lie roughly along an axis from west to east across the Bowland Shale study area, and so can be used to characterise any systematic variations in faulting along this axis.

The Bowland-12 survey was commissioned by Cuadrilla after the HF-IS at the PH well in 2011. The survey area includes the locations of the PH and PNR wells on the Fylde Peninsula. It has therefore been of significant interest and is the subject of several published studies[1,17,49]. The British Geological Survey (BGS) have also published a structural interpretation of this survey[53]. The version of the data used in this study was processed by CGG Veritas in 2012. We use the structural interpretations
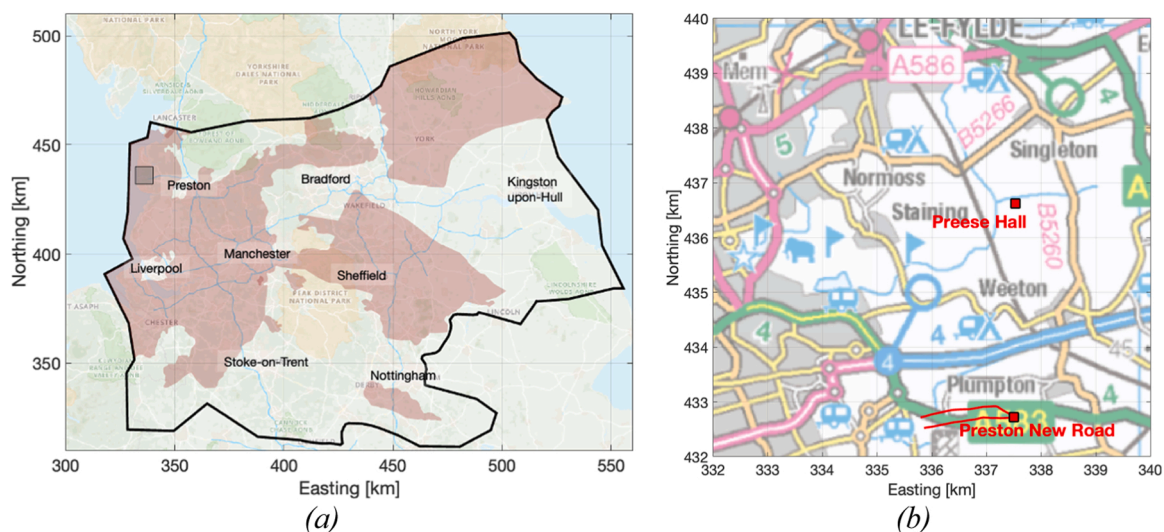

Fig. 1. In (a) we show regions where the Bowland Shale is thought to be prospective based on data from Andrews[2]. The black polygon delineates the region studied by Andrews[2] and the red shaded regions show areas where either the Upper Bowland, Lower Bowland, or both, are considered to be prospective. In (b) we show a map of the region to the east of Blackpool on the Fylde Peninsula (shown as a grey patch in (a)), Lancashire, showing the locations of the three wells (PH-1, PNR-1z and PNR-2) which have conducted hydraulic fracturing in the Bowland Shale. The three wells are all located within approximately 4 km of each other. In both maps, the coordinates are UK National Grid Reference, and the basemaps are sourced from the UK Ordnance Survey.
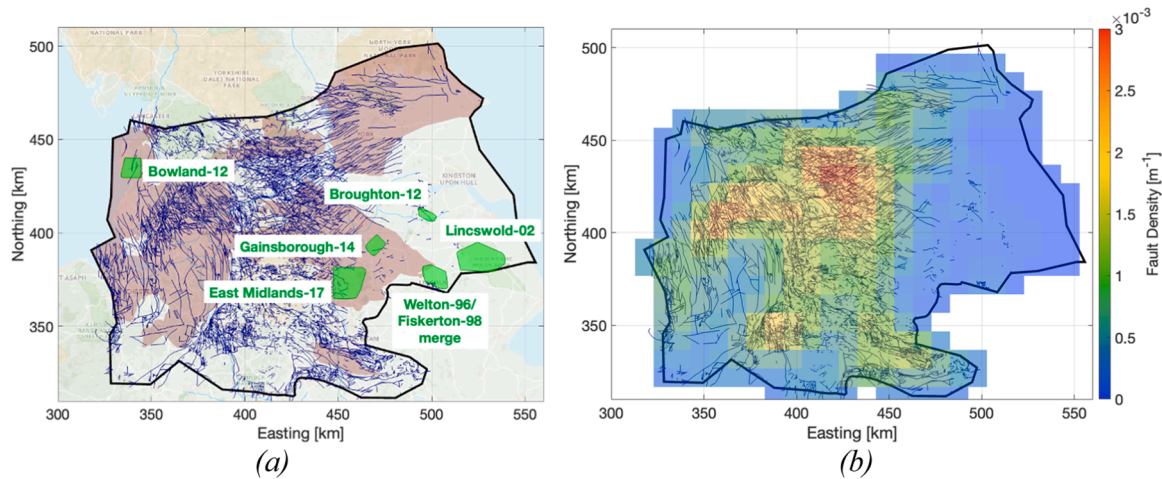
Fig. 2. Regional faulting mapped in northern England. In (a) we show a map of northern England (as per Fig. 1a) showing geological faults from the BGS database mapped at 1:50,000 (blue lines), and the 3D reflection seismic surveys analysed in this study (green polygons). In (b) we show fault densities within 20 × 20 km blocks.

Table 1
3D reflection seismic surveys used in our study.

Survey	Year	Acquisition method	Reprocessed Vintage	Survey area [km²]	CMP bin size [m]	Maximum Acquisition Fold	Interpretation
Bowland-12	2012	Dynamite/ Vibroseis	2012	105	25	150	Randles et al.[53]
Welton-96/Fiskerton-98	1998	Vibroseis	2018	126	30	50	Egdon
Lincswold-02	2002	Vibroseis	2019	300	30	100	Egdon
Broughton-12	2012	Dynamite/ Vibroseis	2015	43	25	67	Egdon
Gainsborough-14	2014	Dynamite	2019	69	25	200	IGas
East Midlands-17	2017	Dynamite/ Hydrapulse	2018	259	25	Not published	None

of the data published by Randles et al.[53].

The Welton-96 and Fiskerton-98 surveys were commissioned by Candecca and Cirque Energy in 1996 and 1998, respectively. These operators were developing conventional resources in this area in the late 1990 s. The areas covered by these two surveys overlap. In 2018 Egdon Resources, who hold oil and gas licenses in the area, commissioned a reprocessed merged dataset that combines the two surveys into a single cube. In this study we use the merged dataset, which was produced by Down Under Geophysics (DUG). We use Egdon Resources' structural interpretation of the data.

The Lincswold-02 survey was commissioned by Roc Oil in 2002, who operated the conventional Saltfleetby gas field in east Lincolnshire. In 2019 Egdon Resources commissioned a reprocessed dataset that was produced by RealTimeSeismic (RTS). In this study we use the reprocessed 2019 data and the structural interpretation of this dataset provided by Egdon Resources. The Broughton-12 survey was commissioned by Egdon Resources. The conventional Wressle oilfield lies within the survey area. The version of the dataset that we use in this study was reprocessed by DUG in 2015, and we use Egdon Resources' structural interpretation of this data. The Gainsborough-14 survey was commissioned by IGas Energy in 2014. IGas Energy were exploring for shale gas resources in this area. The version of the dataset that we use in this study was reprocessed by RTS in 2019, and we use IGas Energy's structural interpretation of this data. The East Midlands-17 survey was commissioned by INEOS in 2017. INEOS were exploring for shale gas resources in this area. The version of the dataset that we use in this study was processed by DUG in 2018. No prior structural interpretation of the dataset was available, and so we performed a brief interpretation of key horizons and structures for this study ourselves.

Fig. 3 shows a stratigraphic column highlighting key formations in the Carboniferous of northern England. Note the variation between basinal and platform regions in the Lower Carboniferous. In the Broughton-12, Lincswold-02 and Welton-96/Fiskerton-98 surveys, the

Lower Carboniferous is represented by platform limestones rather than basinal shales[2]. However, we include them to provide increased spatial coverage across the area of interest, and because hydraulic fracturing of tight gas sandstones, especially within the Namurian-age Millstone Grits, has taken place within these areas[48,63].

In the following sections we extract and plot seismic and fault properties across horizons within each survey. For each survey we use a horizon corresponding to the Lower Carboniferous, either the Bowland Shale or the contemporaneous Visean/Lower Namurian Limestones (see Fig. 3). We also examine a second horizon for each survey through the middle Carboniferous section (either Upper Namurian or Lower Westphalian). Our motivation for doing so is that hydraulic stimulation has also taken place for decades in tight sandstone reservoirs within these horizons (the Millstone Grit Group in particular). No seismicity has been associated with that activity[48], making for an interesting comparison with recent activities in the Bowland Shale. Table 2 specifies in detail the horizons extracted for further analysis from each dataset.

3.2. Structural interpretations and fault offsets

Fig. 4 shows structure maps of Lower Carboniferous horizons for each survey area, with interpreted faults overlain. We use a consistent colour scale range (1.3 s) for each survey area in this figure, which highlights the fact that the topographic range of the Lower Bowland surface in the Bowland-12 survey area is notably larger than equivalent surfaces in the other survey areas. In the Bowland-12 survey, the Lower Bowland surface varies in depth from 0.6 to 1.8 s. In contrast, the other survey areas are significantly flatter, typically with a depth range of only 0.3 – 0.4 s across the entire survey areas. The extent of faulting within the Lower Bowland in this survey is apparent from the interpreted sections presented in Figs. 6 – 10 of Anderson and Underhill[1].

Our first quantification of fault intensity is to examine the offsets of the interpreted faults. Fault length typically scales with offset[19], while
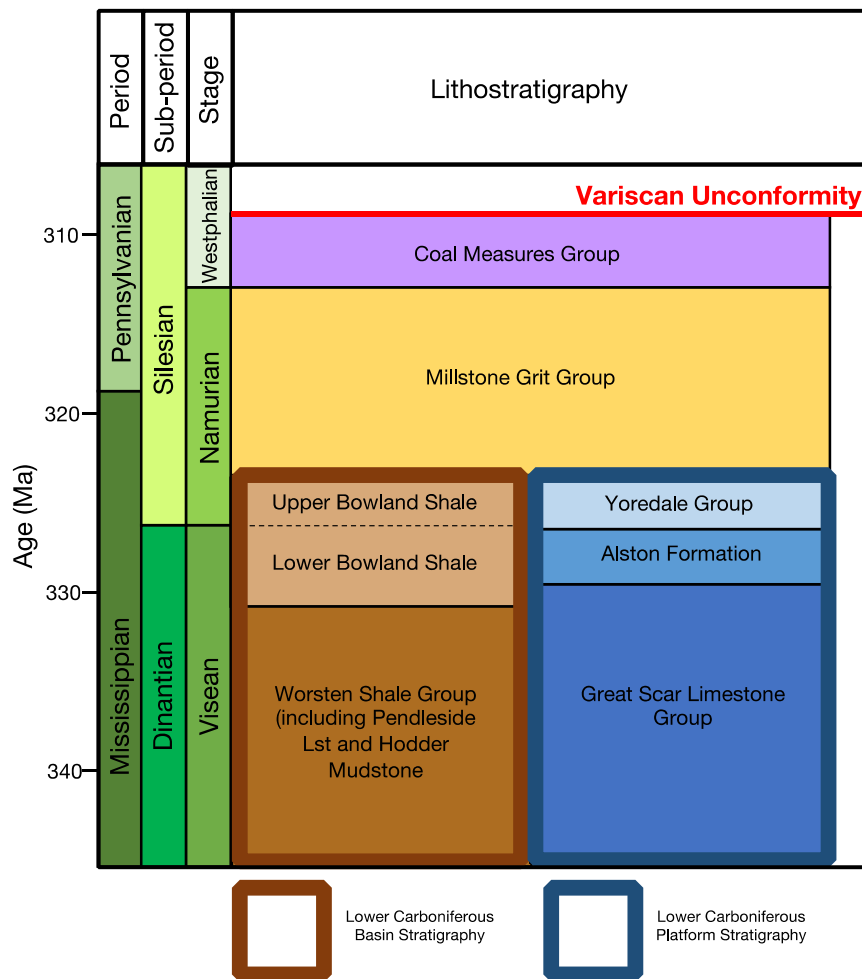
Fig. 3. Stratigraphic column showing the relationships between horizons in the Carboniferous in northern England. Adapted from Anderson and Underhill[1].

Table 2
Horizons extracted from the 3D reflection surveys.

Survey	Middle Carboniferous horizon	Lower Carboniferous horizon
Bowland-12	Pre-Permian unconformity	T = 1200 ms
Welton-96/ Fiskerton-98	Lower Westphalian marker (near base of coal measures)	Top of Visean Limestones
Lincswold-02	Base of Brinsley (middle coal measures)	Top of Visean Limestones
Broughton-12	Ashover Grit	Top of Visean Limestones
Gainsborough-14	Millstone Grit	Lower Gainsborough Shale
East Midlands-17	Surface 230 ms above the top of Visean shales (through Namurian section)	Top of Visean shales

the relationship between fault lengths and fault numbers typically follows a power-law distribution[13]. Hence, we would expect fault densities to scale with the offsets of the largest faults: regions with larger fault offsets might also be expected to have higher intensities of faulting at the sub-seismic scale. This effect could be somewhat modified by basin inversion, whereby reverse motion on faults reduces the overall observed offsets but would further increase faulting intensity. However, we believe that assuming a positive correlation between observed fault offsets and faulting intensity is reasonable.

For each of the faults shown in Fig. 4 we compute the maximum offset within the Lower Carboniferous horizons. The distributions of maximum offsets for each survey are shown in Fig. 5. We find a clear difference between the Bowland-12 survey area and all the other surveys, which reflects the different ranges in subcrop topographies that is immediately apparent in Fig. 4.

The Broughton-12, Lincswold-02 and Gainsborough-14 surveys do not contain any faults with offsets larger than 100 ms, while the Welton-96/Fiskerton-98 survey contains one such feature, with a maximum offset of 120 ms. In contrast, the Bowland-12 survey area contains faults with significantly larger offsets, with 7 having offsets of over 100 ms, and the largest being over 700 ms. In addition to the mapped faults in the Bowland-12 survey, the Woodsfold fault, which is the largest structure in the survey area, has significantly larger offsets such that the presence of the Lower Bowland Shale within the footwall of this fault (the southeast corner of the survey area) is unclear[1]. We have therefore not computed an offset for this structure. Overall, the offsets of interpreted faults within the Bowland-12 survey area clearly indicate that this region may have a significantly higher intensity of faulting relative to the survey areas further to the east.

4. Automated fault mapping

The interpretations shown in Fig. 4 are drawn from manually interpreted horizons and faults. It is well established that seismic interpretation will be affected by the biases of an interpreter, and mapping of small faults at the limits of seismic resolution will be particularly
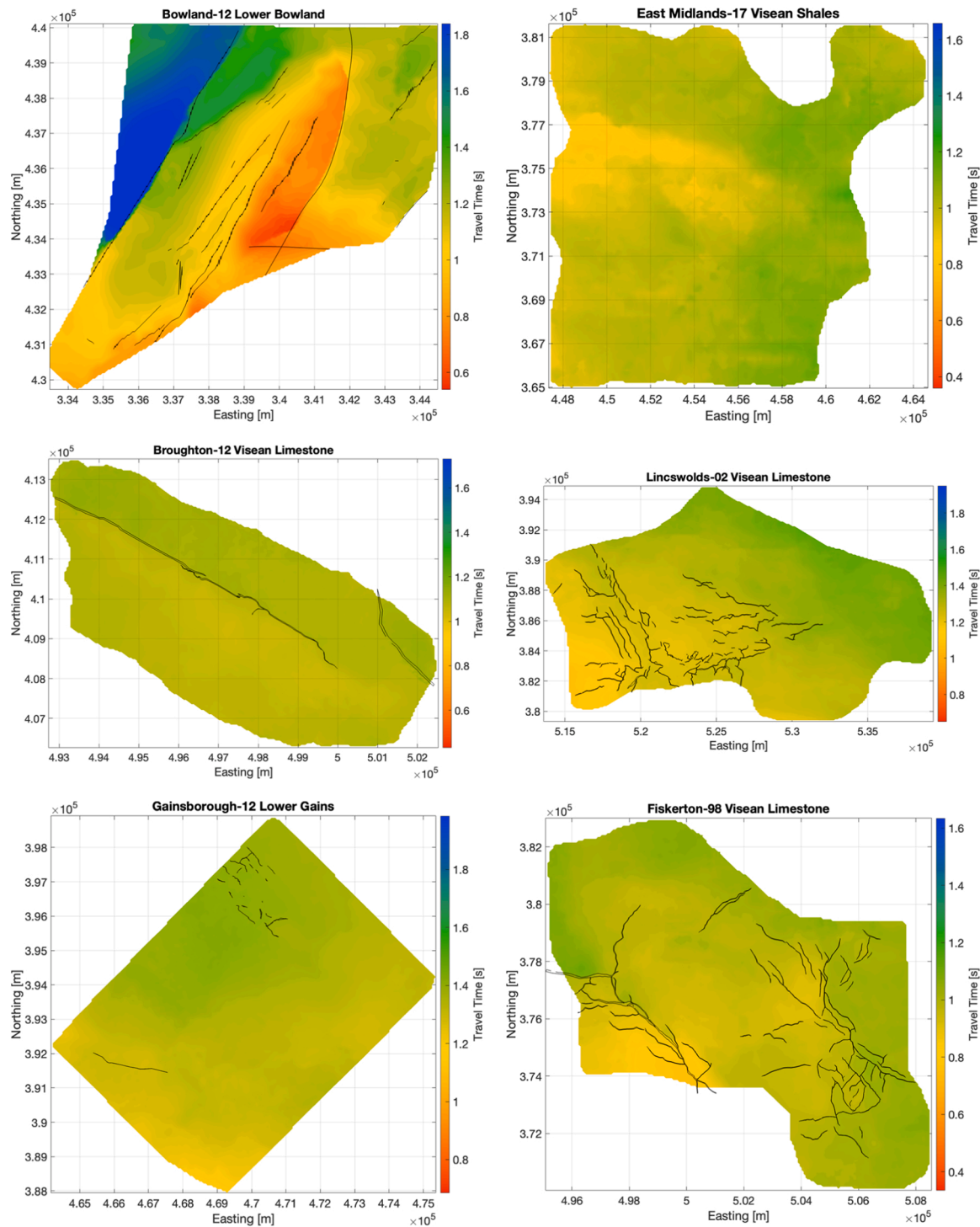
Fig. 4. Structure maps showing Lower Carboniferous interpreted horizons. Black lines show interpreted faults. For all images the colour-scale is defined across a consistent range in order to highlight differences in the scale of subcrop topography between different surveys.

subjective[12]. Since our objective is to compare the abundance of faults between different surveys, we require a method for fault characterisation that minimises the variability that inevitably arises when different interpreters examine different datasets.

Automated fault mapping is an increasingly common tool for seismic interpretation. Since faults create discontinuities in seismic horizons, automated fault mapping is typically based on measures of coherence or semblance[45], or measures of discontinuity such as variance[60], gradient magnitude[3], or curvature[15]. Once fault images have been generated fault surfaces can be automatically extracted using techniques such as

ant-tracking[52].

4.1. Method

In this study we adopted the Thinned Fault Likelihood (TFL) method[32], which we briefly recount here. The TFL is computed from a semblance image, S:
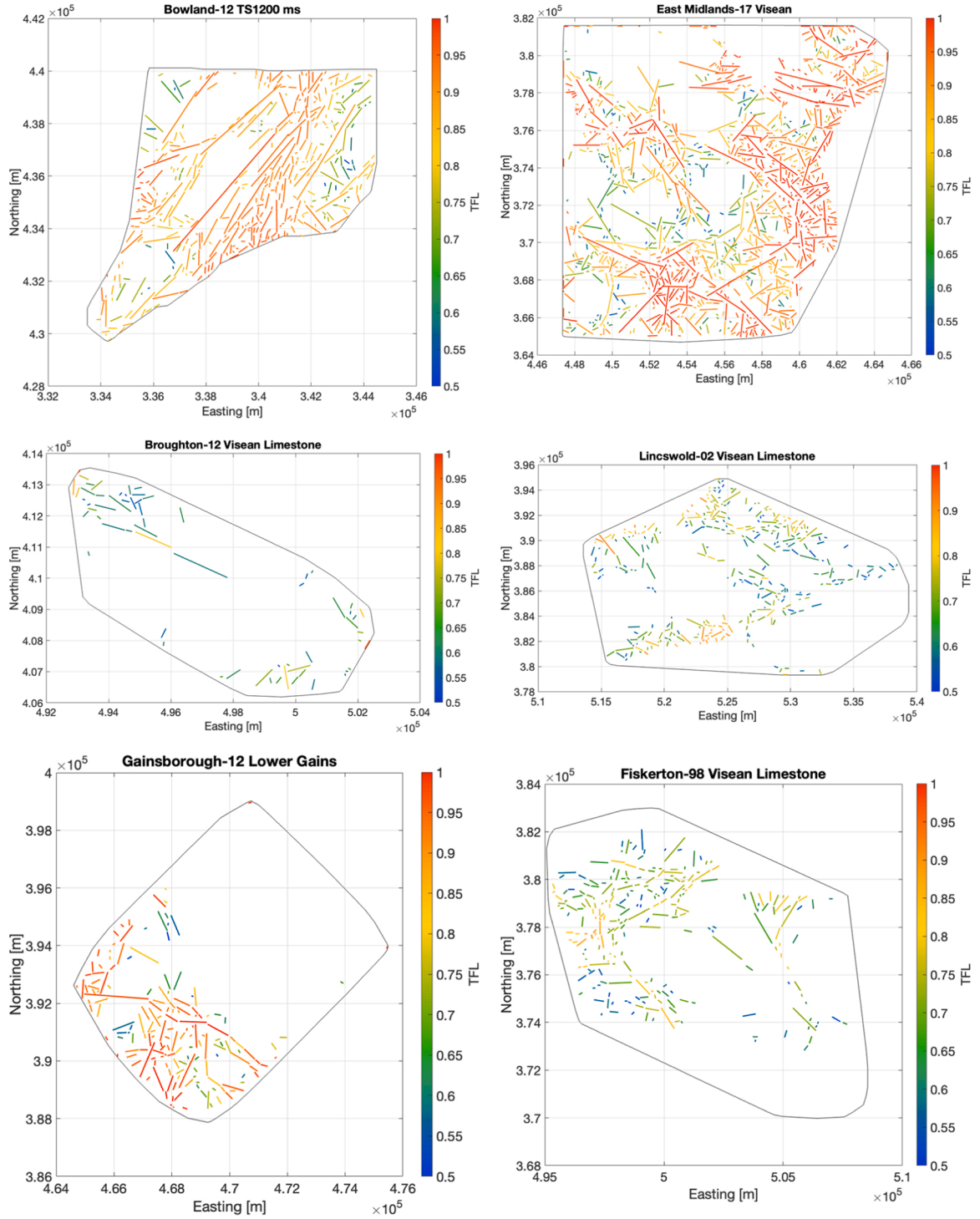
Fig. 6. Fault maps (faults coloured by their maximum TFL value) for Lower Carboniferous horizons for each survey area.

$$S = \frac{\left\langle \langle\text{image}\rangle_s^2 \right\rangle_f}{\left\langle \langle\text{image}^2\rangle_s \right\rangle_f}, \tag{1}$$

where $\langle\bullet\rangle_s$ denotes a structure-orientated averaging of 3×3 voxels of seismic amplitude (centred on the imaging point under analysis), and $\langle\bullet\rangle_f$ denotes a further fault orientated smoothing (see Hale[32] for a detailed explanation of these smoothing terms). Hale[32] then defines fault likelihood as:

$$F_L = 1 - S^8 \tag{2}$$

The choice to raise to the power 8 is arbitrary but serves to increase the contrast between image points with high and low semblance. The fault smoothing term is computed over variable fault strike φ, and dip θ, angles, to find orientations that maximise F_L.

These steps produce a somewhat diffuse cloud of image points with high F_L. The final step is to create thinned fault surfaces from the F_L image. Hale[32] does this by computing the spatial derivatives of F_L: faults are likely to be found at F_L maxima where spatial derivatives are zero. The resulting "ridges" can then be linked together in 3 dimensions, creating fault surfaces. In our study, we implemented our TFL analysis
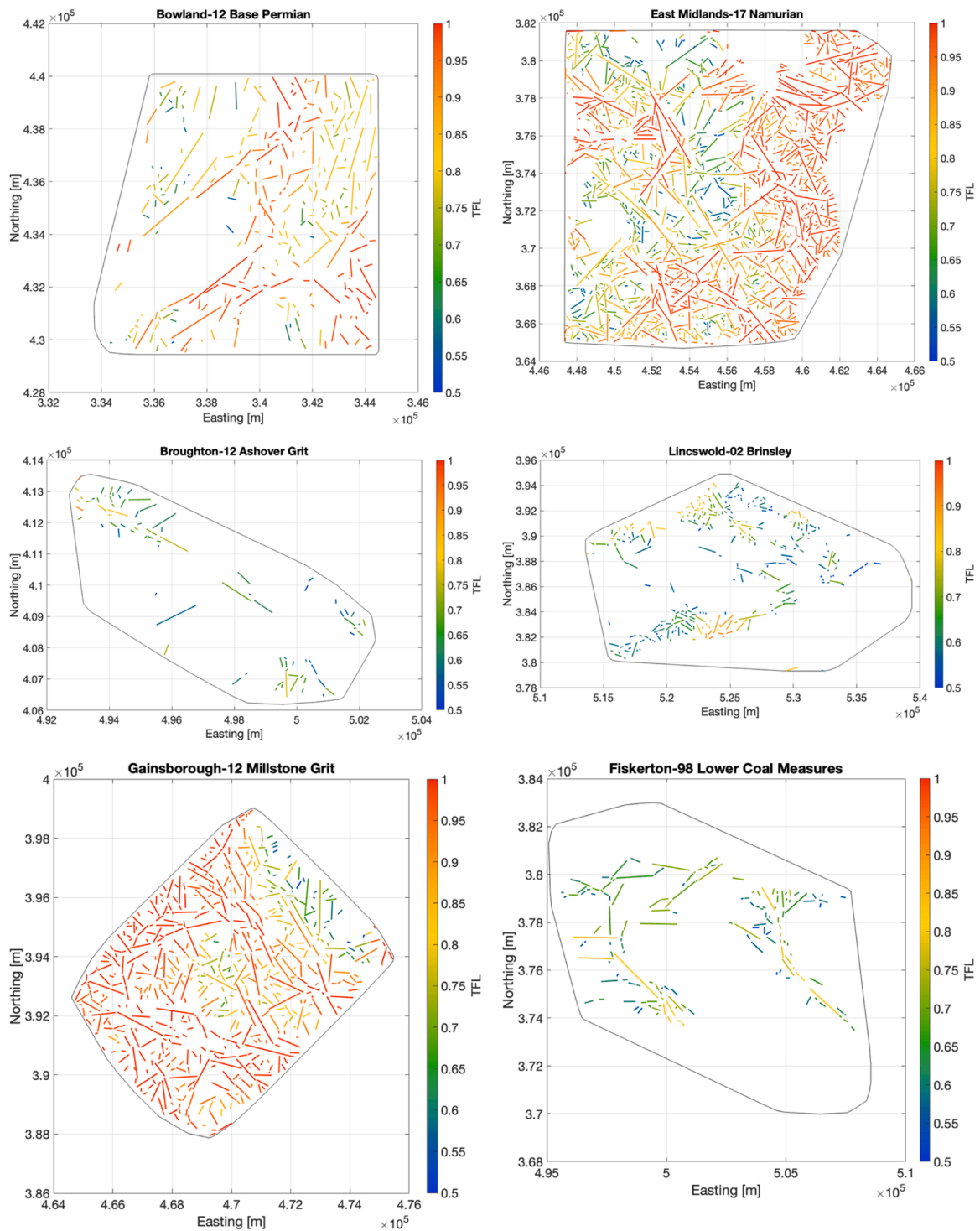
Fig. 7. Fault maps (faults coloured by their maximum TFL value) for Middle Carboniferous horizons for each survey area.

using the built-in attribute within the *OpendTect* seismic interpretation package.

We used a clustering algorithm (DBSCAN[25]) to identify the individual faults created by the TFL attribute. We computed the lateral length of each fault within the horizon, and the average fault strike, by approximating each fault as a single planar structure. We used TFL ≥ 0.5 as an arbitrary cut-off, rejecting structures for which TFL < 0.5 across all imaging points. In the following figures, for each fault we show the maximum TFL value along that structure.

4.2. Results

Figs. 6 and 7 show the resulting fault maps for each of the analysed surveys. We found good overlap between features with higher TFL values and manually interpreted faults, but the TFL attribute identified many smaller features that are not mapped in Fig. 4. Fig. 8 shows histograms of fault length for each of the identified horizons, normalised by the survey areas. We would expect fault length distributions to follow a power law[13]. However, plotted in log-log space, all of the curves have a slightly convex shape, suggesting that some smaller faults are missed by
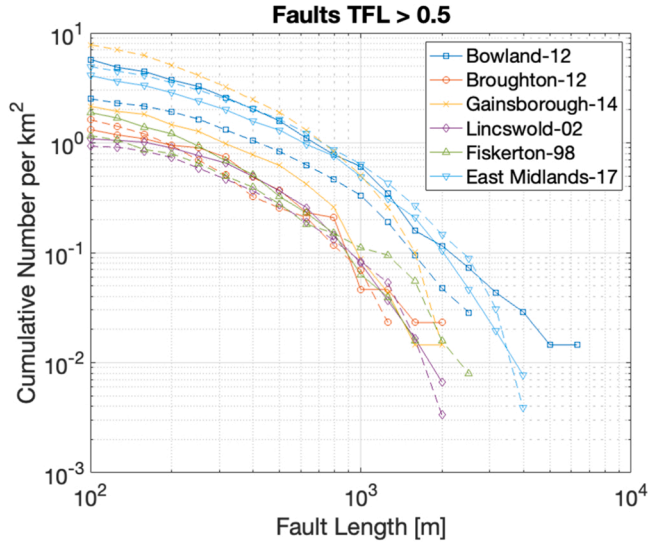
Fig. 8. Cumulative histograms of fault length, normalised by survey area, for each of the extracted survey horizons. Solid curves show fault lengths in the Lower Carboniferous, and dashed curves show fault lengths in the mid Carboniferous horizons.

our analysis. However, the degree of convexity is similar for all of the survey histograms, suggesting that any bias that could be introduced by a lack of fault detection will be similar for each survey.

We do not identify any systematic difference in the intensity of faulting between Lower and Middle Carboniferous horizons. The Gainsborough-14 survey has more faulting on the Millstone Grit horizon than the Lower Gainsborough Shale, while the Bowland-12 survey has more faulting on the Bowland Shale time horizon than the Upper Namurian surface. The other surveys have similar intensities of faulting on both surfaces. This is to be expected, given that both Lower and Middle Carboniferous formations will have experienced the same tectonic events (namely the Variscan Orogeny, post-Variscan extension in the Mesozoic, and Tertiary uplift). Hence, any observed differences in HF-IS prevalence between hydraulic fracturing in the Lower Carboniferous shales versus the Millstone Grits is unlikely to be a product of lower faulting intensity.

We find roughly an order of magnitude difference in Lower Carboniferous fault densities between the different surveys. The Bowland-12 survey has the highest fault density, followed by the East Midlands-17 and Gainsborough-14 cases. The Welton-96/Fiskerton-98, Lincswold-02 and Broughton-12 cases have the lowest fault densities. This trend matches the inferences drawn from the BGS fault mapping (Fig. 2) and from Figure 42 of Andrews[2], and from our assessment of the offsets on interpreted faults (Fig. 5), namely that fault density decreases along a west-to-east axis.

5. STRESS AND pore pressure gradients

Having mapped the presence of faults within each survey, we then need to assess whether the mapped faults are critically stressed and therefore may be likely to host induced seismicity. This requires us to resolve the in situ stresses onto each surface to compute effective shear and normal stresses.

5.1. Data

Data pertaining to stress and pore pressure gradients within Lower Carboniferous strata in northern England is scarce. Kingdon et al.[41] compiled S_{Hmax} orientations (θ_{SHMAX}) collated from a selection of boreholes across the region and Fellgett et al.[28] provide stress and pore

pressure gradients. Fellgett et al.[28] show that the stress regime in the region is broadly strike-slip, with $S_{Hmax} > S_V > S_{Hmin}$. They define two separate stress regions – East Yorkshire/North Nottinghamshire (to the east of the Pennines), and Cheshire/Lancashire (to the west of the Pennines), and estimate stress representative stress gradients of:

- $\Delta S_V = 0.023$ MPa/m; $\Delta S_{Hmin} = 0.01475$ MPa/m for East Yorks./ North Notts., and
- $\Delta S_V = 0.025$ MPa/m; $\Delta S_{Hmin} = 0.0174$ MPa/m for Ches./Lancs.

However, there is a large amount of scatter in these measurements. Fellgett et al.[28] also collated pore pressure gradients, finding that they are mostly near hydrostatic ($\Delta P \approx 0.010$ MPa/m). However, Fellgett et al.[28]'s values were drawn exclusively from formations above the Bowland Shale, whereas the only pore pressure measurements from within the Bowland Shale showed that this formation was over-pressured ($\Delta P \approx 0.013$ MPa/m)[39]. Fellgett et al.[28] also showed ΔS_{Hmax} measurements, but found significant variability, and they did not attempt to estimate average or representative values.

For the Bowland-12 survey area, stress gradients have been relatively well constrained from the hydraulic fracturing activities in the PH and PNR wells. In this study we adopt the values used by Kettley et al.[39] of $\Delta S_V = 0.025$; $\Delta S_{Hmin} = 0.0164$; $\Delta S_{Hmax} = 0.032$ MPa/m; and $\theta_{SHMAX} = 172°$.

We also have well-constrained stress gradients from recent (2021) hydraulic fracturing in the Wressle oilfield (within the Broughton-12 survey area), as described by Verdon[63]: $\Delta S_V = 0.0242$; $\Delta S_{Hmin} = 0.0186$; $\Delta S_{Hmax} = 0.032$ MPa/m, and $\theta_{SHMAX} = 147°$. We adopt these values for the Broughton-12, Welton-96/Fiskerton-98 and Lincswold-02 survey areas.

For the Gainsborough-14 and East Midlands-17 survey areas, we have an additional data point from the nearby Mattersey Quarry, where hydraulic fracturing in coal formations was conducted at depths of up to 1000 m (Fellgett, *pers. comm.*), producing average measurements of $\Delta S_V = 0.0248$; $\Delta S_{Hmin} = 0.0145$; $\Delta S_{Hmax} = 0.0271$ MPa/m, and $\theta_{SHMAX} = 142°$. For the Gainsborough-14 and East Midlands-17 survey areas, we adopt an average value between the Wressle and Mattersey Quarry data points, producing $\Delta S_V = 0.025$; $\Delta S_{Hmin} = 0.0166$; $\Delta S_{Hmax} = 0.0296$ MPa/m, and $\theta_{SHMAX} = 144°$.

We do not have any data with which to establish whether the Bowland Shale is over-pressured throughout its extent. This is a major source of uncertainty in our analysis since the presence of overpressure can significantly affect the susceptibility of a formation to induced seismicity[23]. We note that there is an inherent trade-off where high pore pressures are considered beneficial with respect to the economic production of hydrocarbons, but detrimental with respect to increasing the likelihood of experiencing induced seismicity.

In the following analysis, we assume that $\Delta P = 0.013$ MPa/m for all the Lower Carboniferous horizons (matching the PNR observations) and adopt $\Delta P = 0.010$ MPa/m for the shallower horizons, following the observations presented by Fellgett et al.[28]. In general, the relative paucity of stress and pore pressure data within the Bowland Shale produces the largest uncertainties in our analysis. Addressing this lack should be a key focus of future efforts to assess potential HF-IS hazard in the UK.

5.2. Critical pore pressures

Having estimated the in situ stress conditions, we resolve the effective stress tensor into effective normal stress, σ'_n, and shear stress, τ, acting on each fault in order to compute the critical pore pressure, P_C, which describes the pore pressure increase required to generate slip in the absence of cohesion on the fault:

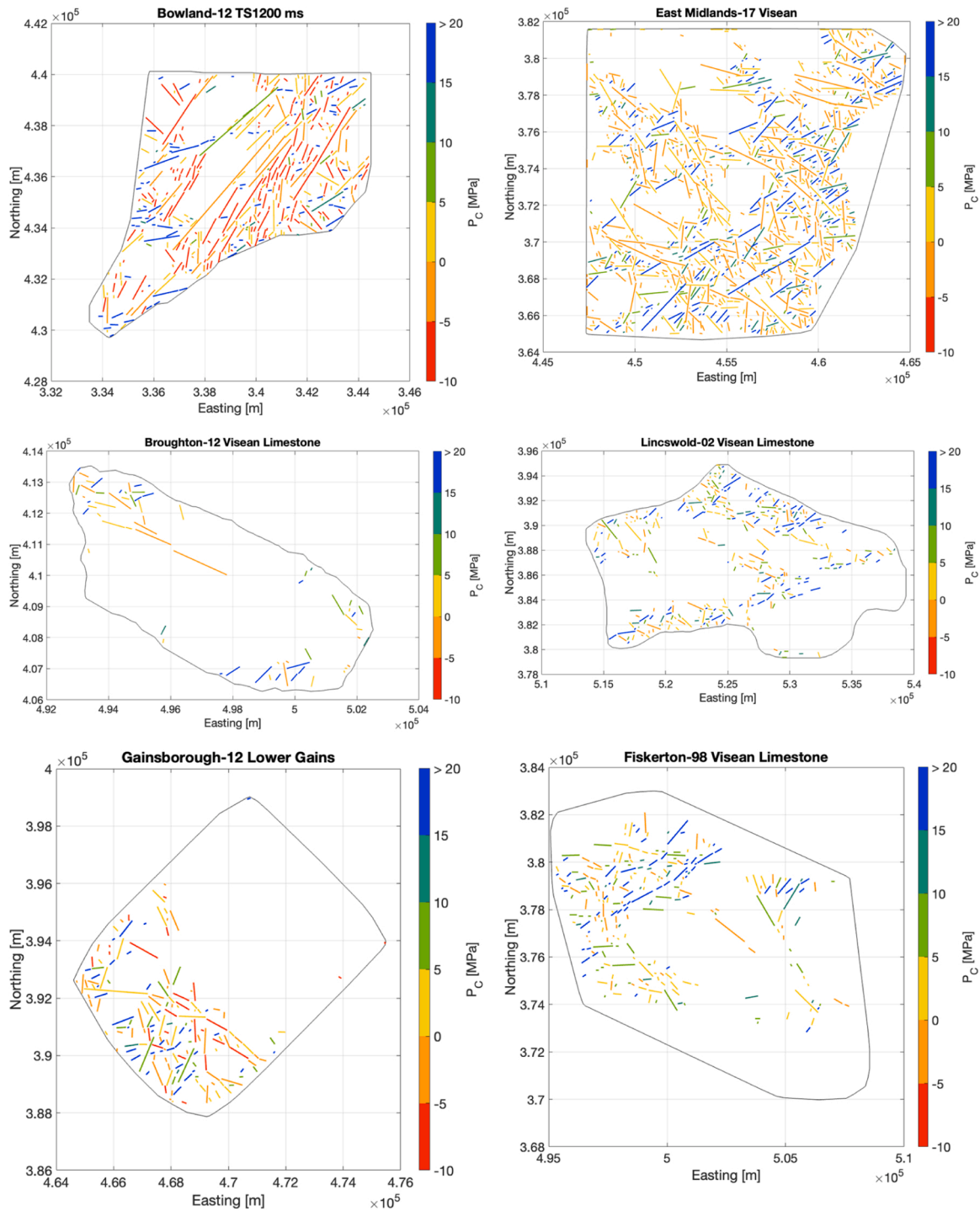$$P_C = \sigma'_n - \frac{|\tau|}{\mu_f}, \tag{3}$$

Fig. 9. Critical pore pressures (P_C) for all mapped faults in the Lower Carboniferous horizons for each survey area.

where μ_f is the coefficient of friction. We assume a generic value of $\mu_f = 0.6$ throughout our analysis. In doing so, we note that, while this value is probably appropriate for the rock mass, substantially lower values may be more appropriate for slipping faults[54,40]. Increasing or decreasing our assumed μ_f value would change the overall numbers of critically-stressed faults, but it would not change the relative proportions between the different survey areas, so long as a consistent value is used. Further work to constrain appropriate values of μ_f for the relatively dormant faults that run through the Bowland Shale would be very useful in better constraining the potential induced seismicity hazard.

From a physical perspective, P_C should always be positive prior to

injection, otherwise the faults would be slipping under natural conditions. However, in practice, negative P_C values are often obtained, likely representing natural variation in frictional parameters and stress conditions, and non-zero cohesion. Kettlety et al.[39] estimated that the fault responsible for the M_L 2.9 induced seismic event during stimulation of the PNR-2 well had $P_C = -3.0$ MPa. We therefore treat values of $P_C < 0$ as indicating that a fault is critically stressed, with minimal pore pressure change required to generate slip. Note that the generation of slip does not necessarily imply induced seismicity, as faults can release strain as a series of smaller magnitude microseismic events, or even slip slowly without generating any radiated seismic energy[27]. Figs. 9 and 10
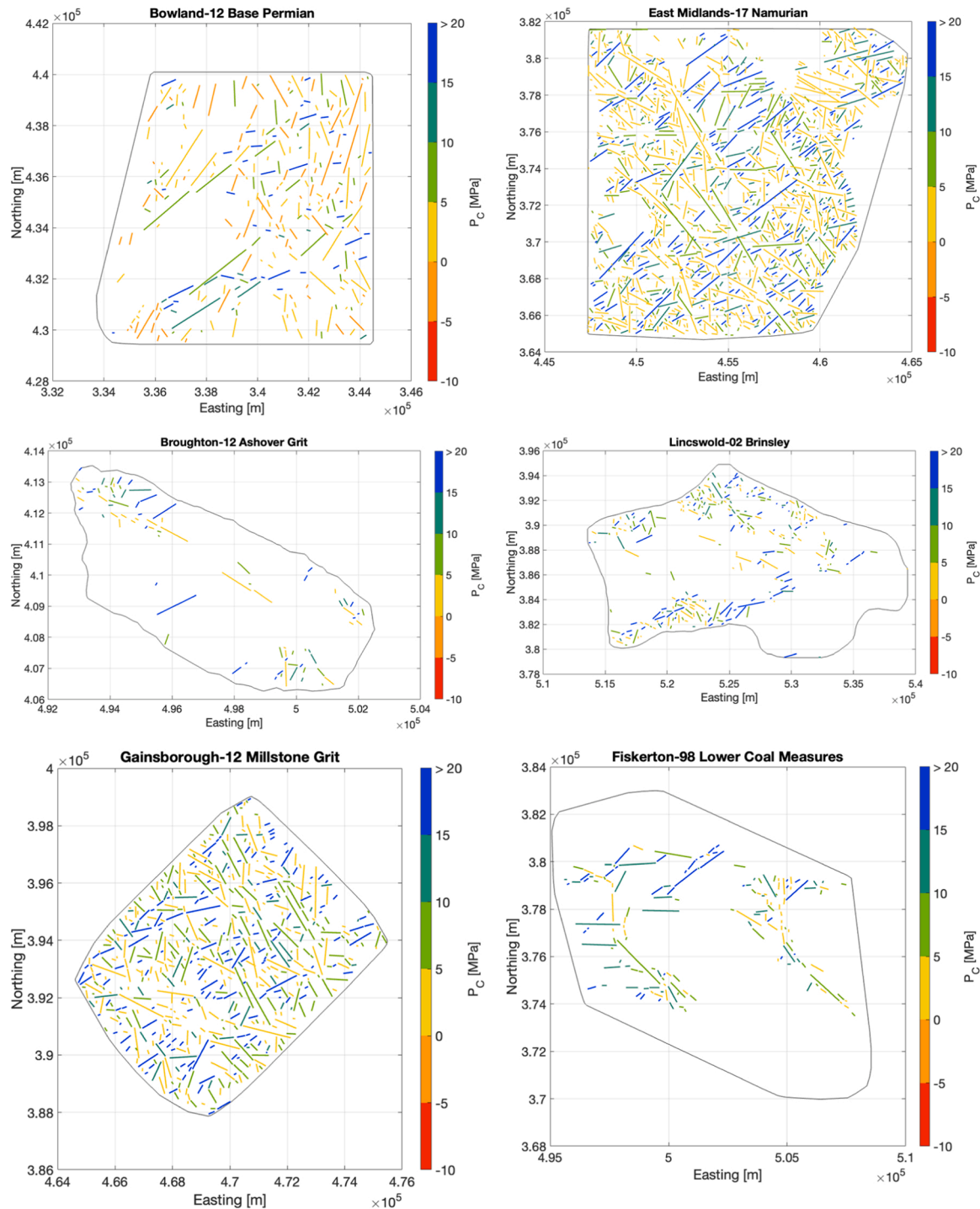
Fig. 10. Critical pore pressures (P_C) for all mapped faults in the mid-Carboniferous horizons for each survey area.

show the P_C values computed for faults within the Lower and Middle Carboniferous horizons for each seismic survey. Fig. 11 shows histograms of critically stressed fault lengths (i.e., faults for which $P_C \leq 0$) for each of the identified horizons, normalised by the survey areas.

The Bowland-12 survey was the only case to have any critically stressed faults within the Middle Carboniferous horizons. Since we assumed identical stress gradients for Lower and Middle Carboniferous horizons, and since there was no overall systematic difference in fault density (see Fig. 8), the absence of critically stressed faults in the Middle Carboniferous is clearly a product of the hydrostatic pore pressures that we adopted[28], versus our assumption of overpressure in the Bowland

Shale. This observation serves to demonstrate the potential impact of elevated pore pressures on the prevalence of HF-IS[23].

From Fig. 11 we observe significant variability in the density of critically stressed faults between the different survey areas. The density is highest for the Bowland-12 survey, with the East Midlands-17 and Gainsborough-14 surveys being factors of 2 and 3 times lower, and the fault densities in the Lincswold-02, Fiskerton-98 and Broughton-12 surveys, furthest to the east, being an order of magnitude lower. These trends match our inferences from the BGS fault mapping (Fig. 2), from the offsets of the larger interpreted faults (Figs. 4 and 5), and from Figure 42 of Andrews[2]; namely that the intensity of faulting does
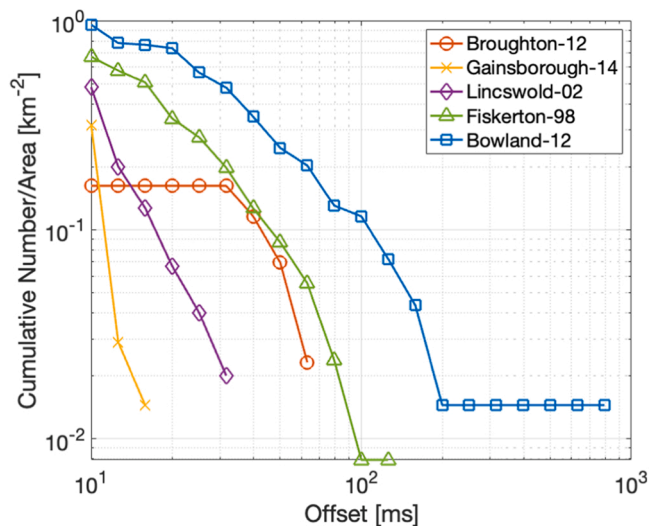
Fig. 5. Distribution of maximum offsets across manually interpreted faults in lower Carboniferous horizons for each survey area.
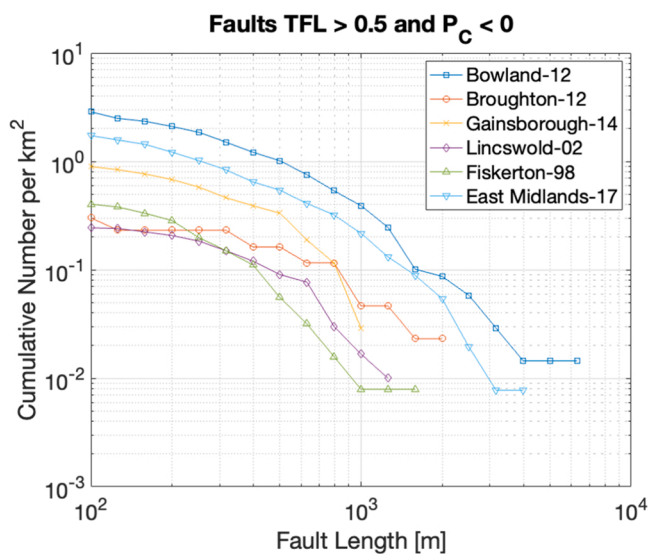

Fig. 11. Cumulative histograms of critically stressed fault length, normalised by survey area, for each of the extracted survey horizons. All curves are for the Lower Carboniferous horizons.

decrease along a west-to-east axis through the Bowland Shale study area.

5.3. Spatial variability in the density of critically stressed faults

In addition to the overall density of critically stressed faults, it is of interest to examine the spatial variability in the density of critically stressed faults. From Fig. 9 we see that some surveys have broad areas with no identified critically stressed faults, while others have faulting across the entire survey area. In Fig. 12 we map the density of critically stressed faults across each survey for the Lower Carboniferous horizons (since there are few or no critically stressed faults in the Middle Carboniferous for any of the surveys). We generate these maps across grids with a spacing of 500 m. For each grid point we compute the density of faulting within a 1×1 km square centred on the grid point – the colouring of each "box" in Fig. 12 denotes the density of critically stressed faults within that square (total length of all critically stressed faults within a block divided by the area of the block). From Fig. 9 the

ubiquity of faulting across the Bowland-12 survey area, in comparison to the other survey areas, is immediately apparent, as is the greater density of faulting in some of the Bowland-12 blocks when compared to any blocks in the other surveys.

Fig. 13 shows histograms of the distributions of critically stressed fault densities for each survey area. We see that the Broughton-12, Gainsborough-14, Lincswold-02 and Welton-96/Fiskerton-98 surveys all have at least 60% of blocks with a fault density of 0 (i.e., no critically stressed faults). The East Midlands-17 survey has over 21% of blocks with no faults, while only 11% of blocks of the Bowland-12 survey have no faults. The apparent ubiquity of critically stressed faults observed in the Bowland-12 survey may explain why the three wells hydraulically fractured within this area each experienced HF-IS.

From Fig. 13 we note that the Broughton-12, Gainsborough-14, Lincswold-02 and Welton-96/Fiskerton-98 surveys do not have any blocks with fault densities higher than $0.002 \, \mathrm{m}^{-1}$, while the East Midlands-17 survey has only one block with density higher than $0.003 \, \mathrm{m}^{-1}$. In contrast, the Bowland-12 survey has 8% of blocks exceeding this density, with the highest densities reaching over $0.0045 \, \mathrm{m}^{-1}$. In combination, these observations further reinforce the fact that the levels of critically stressed faulting within the Bowland-12 survey, which has experienced HF-IS, are both higher and more ubiquitous within this survey area than any other survey in our analysis.

6. IMPLICATIONS FOR HF-IS occurrence

6.1. Deterministic screening for induced seismicity potential

Having observed the variability in abundance of critically stressed faults across the Bowland Shale play, we can examine how this might influence the likelihood of generating HF-IS. In theory, it might be possible to use the fault observations presented here to generate geomechanical simulations of subsurface perturbations. These models could then be used to screen a proposed site for induced seismicity potential. This type of deterministic approach, where faults are mapped and a "respect distance" defined whereby hydraulic fracturing does not take place within proximity to mapped faults, has been proposed by several studies[20,71,72].

In practice, however, this deterministic screening approach has proved challenging. Wellbore-based methods have a small radius of investigation around the well, limiting their utility for fault detection. As such, 3D seismic reflection surveys provide the most comprehensive and complete geophysical coverage of the subsurface with which to identify faults. However, the resolution of 3D surveys is typically of the order of 10 s of metres. Nantanoi et al.[49] lists the fault area, length and offset required to host an earthquake of a given magnitude, based on typical earthquake-fault scaling parameters. A fault capable of hosting an M_L 3.0 earthquake may have a displacement of only 3 m. Faults are detected in 3D seismic surveys by their offset, so only faults with offsets larger than the 3D seismic resolution can be robustly identified and mapped. Faults capable of hosting magnitude M_L 3.0 or even M_L 4.0 events may be below the seismic resolution, and so be missed by a deterministic attempt to screen for seismogenic faults. Furthermore, detection of faults in 3D seismic surveys relies primarily on the presence of vertical offsets. Strike slip faults may only generate lateral offset, which can be challenging to identify with 3D reflection seismic surveys, regardless of the seismic resolution.

In addition to the challenge of identifying faults, fault reactivation will be strongly dependent on the frictional properties of the faults, as quantified by the friction coefficient and cohesion, as well as parameters that describe the dynamic behaviour of the fault. Such parameters are likely to be very poorly constrained by site characterisation efforts prior to the start of operations. The positions of reactivated faults become clear once induced seismicity begins to occur[50], and observed seismicity can be used to estimate the geomechanical properties of faults[40]. However, by definition these methods require the induced seismicity
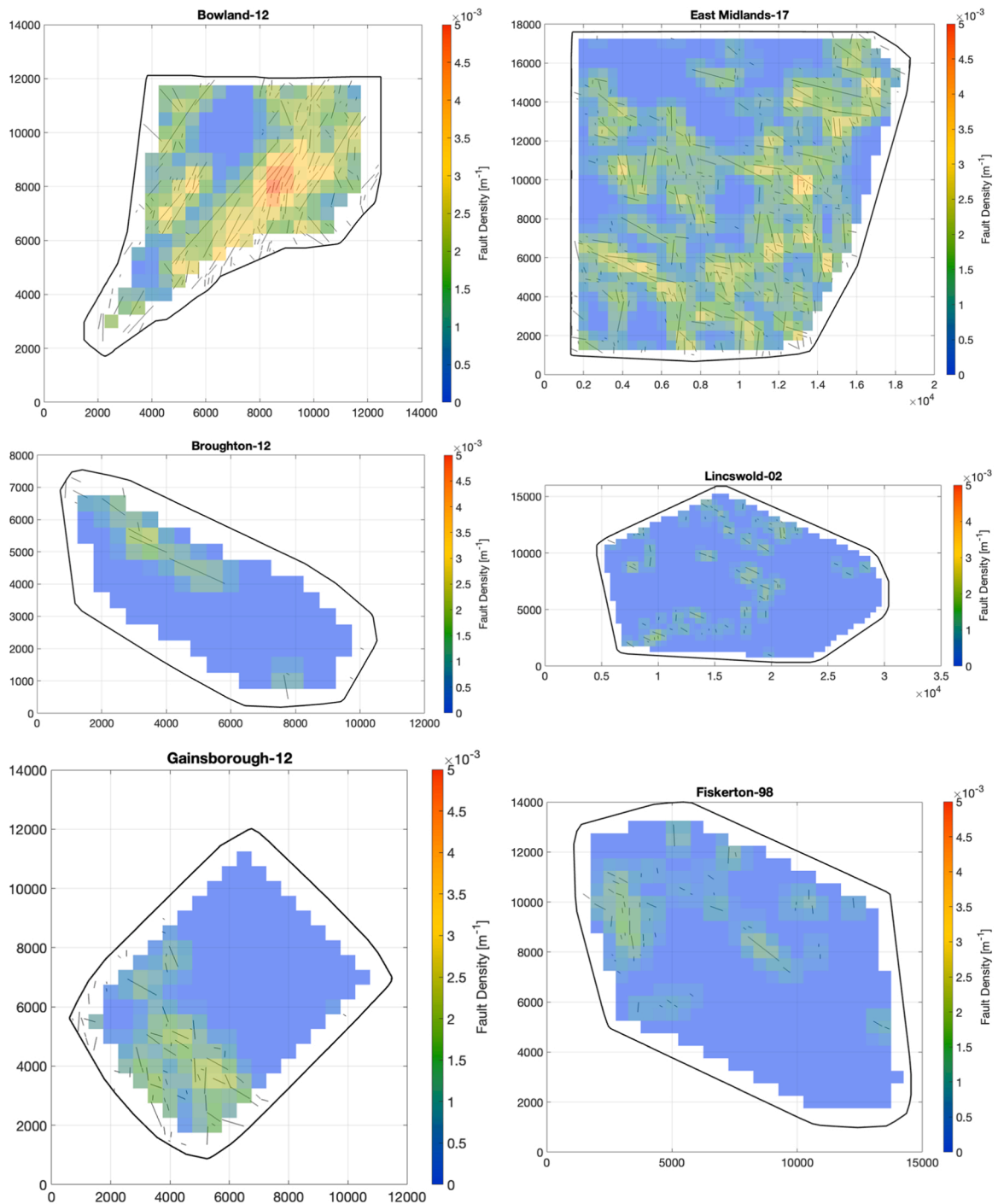
Fig. 12. Maps of critically stressed fault densities across each survey area. All maps are for lower Carboniferous horizons. The colours show the fault density within each block, while the black lines show the critically stressed faults.

sequence to have begun, and so they cannot inform attempts to quantify the induced seismicity hazard using deterministic methods prior to the start of operations.

The PNR wells in Lancashire, UK, provide a case example of the challenges of relying on a priori geophysical observations to avoid HF-IS. The stimulation was monitored using downhole microseismic arrays, which allowed us to image the interaction between the developing hydraulic fractures and any pre-existing structures. The faults that reactivated to generate the HF-IS with magnitudes of M_L 1.5 (PNR-1z) and M_L 2.9 (PNR-2) can be clearly imaged with the microseismic data[18,37,39]. However, the structures identified with the microseismic

monitoring do not correspond to the faults mapped in the 3D seismic and there are no clear or identifiable structures in the 3D seismic that could indicate the presence of faults at the positions indicated by the microseismicity[49]. Clearly, the faults responsible for the PNR HF-IS were either below the limits of reflection seismic resolution or were strike slip faults that did not generate vertical offsets.

The ToC2ME dataset[24,36] from Fox Creek, Alberta, provides a similar case study. Several faults were identified using 3D seismic reflection data. However, while the mapped faults did not produce any seismicity, the fault which caused the induced seismicity was not visible in the 3D seismic data.
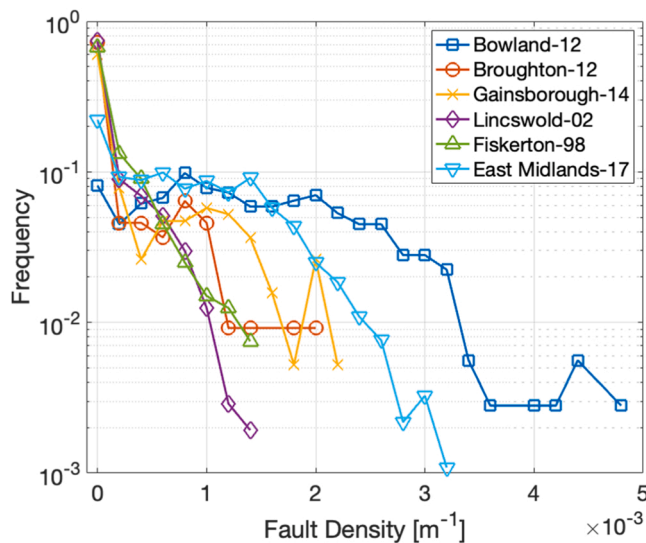
Fig. 13. Histograms of fault density across each survey area (normalised by the total number of measurement points for each survey).

These cases show that faults responsible for HF-IS may not be visible in 3D seismic reflection data. If we cannot identify the causative faults using geophysical imaging methods, then clearly it will not be possible to generate accurate geomechanical models to evaluate whether a given subsurface activity will reactivate them. Hence, with our current geophysical imaging capacity a deterministic approach to the mitigation of HF-IS, as proposed by Westwood et al.[71], Wilson et al.[72], and de Jonge-Anderson et al.[20], does not appear to be practicable.

Instead, our view is that a probabilistic approach to induced seismicity hazard assessment is more appropriate. We can use fault scaling relationships based on the observed seismic-scale faults to infer the expected distribution of sub-seismic scale features (and to compare and contrast between different survey areas). We can then use these distributions to assess the potential hazard by considering the likelihood that hydraulic fracturing intersects and reactivates a critically stressed fault.

6.2. Estimates of maximum magnitude

An important factor when evaluating the seismic hazard posed by HF-IS is to establish appropriate constraints on M_{MAX}^P, the magnitude of the largest earthquake considered physically possible. M_{MAX}^P describes the largest event that could physically be triggered by the activity in question[10].

McGarr[46] proposed that the largest earthquake is limited by the total volume of injected fluid, where:

$$M_{MAX}^P = G\Delta V, \tag{4}$$

where G is the rock shear modulus, and ΔV is the injected volume. However, some cases of induced seismicity have exceeded this threshold[6], indicating that it probably does not provide a robust estimate for M_{MAX}^P. Van der Elst et al.[61] argued that, while the volume controls the number of earthquakes, the size of the largest possible earthquake is determined by the tectonics of the region. The findings of van der Elst et al.[61] have been used to suggest that M_{MAX}^P for HF-IS should be the same as that used for tectonic earthquakes.

For standard seismic hazard assessment of tectonic earthquakes, M_{MAX}^P defines the largest earthquake that could occur given the current tectonic setting. For HF-IS, the question is different since the subsurface perturbation is limited in both time and space. We must therefore consider the largest earthquake that could be triggered during the short-lived period of injections within the volume of rock perturbed by the stimulation, which is relatively small on a crustal scale, albeit

recognising that the presence of permeable fracture zones within otherwise low permeability shales[36] and poroelastic stress transfer[35,37, 38] can increase the perturbed region significantly beyond the extent of the hydraulic fractures themselves.

It may therefore be appropriate to use M_{MAX}^P values for induced seismicity that are different to values adopted for tectonic seismic hazard[10]. This has often been done in practice. For example, Atkinson et al.[5], in a study of induced seismicity hazard in the WCSB, adopted a logic tree for M_{MAX}^P of hydraulic fracturing-induced events ranging from $4.5 > M_{MAX}^P > 6.5$, with a 70% likelihood that $M_{MAX}^P \leq 5.0$. In contrast, the regional tectonic M_{MAX}^P used by the Geological Survey of Canada for the plains and foothills of the WCSB is M 7.0, two orders of magnitude larger. No hydraulic fracturing-induced earthquake in the WCSB has yet exceeded M 5.0, despite extensive use of high-volume hydraulic fracturing in shale plays in this basin[65].

For the Groningen gas field in the Netherlands, where seismicity is driven by compaction of a large, mature gas reservoir, the tectonic M_{MAX}^P in the Groningen region is estimated to be ≥ 6.5[73]. In contrast, studies of induced seismicity at Groningen have proposed M_{MAX}^P values for induced seismicity in the range of $4.0 - 4.5$[8,21,75], and the largest observed earthquake to date was M_L 3.6. Bommer and van Elk[11] developed a logic-tree for Groningen that yielded a probability of less than 10% that M_{MAX}^P for induced seismicity is the same as M_{MAX}^P for tectonic seismicity.

In the United States, the USGS uses a value of M_{MAX}^P for tectonic earthquakes in the central and eastern US of 7.0[47], but no HF-IS in this region has yet exceeded a magnitude of 5.0[65,66]. Mancini et al.[44] adopted the UK tectonic M_{MAX}^P of M 6.5 as the basis for their study into the PNR seismicity, although their modelling did not constrain this parameter, and their results were not sensitive to this choice. Their adoption of the regional tectonic value represents an outlier with respect to assessment of HF-IS elsewhere.

The role of M_{MAX}^P in seismic hazard assessment is to remove the contribution of unfeasibly large magnitudes that would otherwise be generated by an unbounded extrapolation of the Gutenberg-Richter distribution[10]. Hence, its significance will depend on whether events of that size are in play given the estimated recurrence parameters. If events of a size within a range of possible M_{MAX}^P choices are considered very unlikely to occur based on the expected recurrence, then the choice of M_{MAX}^P value becomes relatively unimportant. This was in fact the case for the Mancini et al.[44] PNR study – while they chose an M_{MAX}^P of M 6.5, the likelihood of events larger than M 3.0 generated by their model-based forecasting was very small, and so their choice for the M_{MAX}^P parameter was immaterial.

A key issue in the consideration of appropriate M_{MAX}^P values for induced seismicity is depth of earthquake nucleation. Large earthquakes tend to occur at mid-crustal depths, with a large portion of the rupture propagating upwards from the hypocenter[43]. For the case of fluid injections associated with hydrocarbon activities, events typically occur in the sedimentary column, or within the uppermost portion of the underlying basement[62]. Levels of induced seismicity from activities in formations that are isolated from basement strata are often substantially reduced[59,66,67]. Since the sedimentary cover will be rheologically softer and weaker, and have lower in situ stresses[69], it is unlikely that these layers will be physically capable of hosting earthquakes as large as those that occur naturally at greater depths, and therefore the regional tectonic M_{MAX}^P is not an appropriate value for the M_{MAX}^P for HF-IS.

Green et al.[30] used observations from past coal mining-induced seismicity as their basis for estimating M_{MAX}^P for HF-IS in the Bowland Shale. Their argument was that the largest seismicity during the very large disturbances created by longwall coal mining never exceeded magnitude M 3.0, and hence it was not possible that hydraulic stimulation, which represents a far smaller subsurface disturbance than mining, would exceed this. However, seismicity during stimulation of the PNR-2 well reached M_L 2.9: while marginally below the Green et al.[30] threshold, the PNR-2 seismicity has reduced the confidence in this value.

Most coal mining in the UK took place at depths within 1 km of the ground surface, whereas hydraulic stimulation in the Bowland Shale took place at over 2 km depth at PNR. It is therefore arguable whether past mining-induced seismicity can really be used as a proxy to estimate M_{MAX}^P for hydraulic fracturing-induced events. Moreover, the mechanism of deformation that generated mining induced events in the UK was generally roof collapse above longwall panels, resulting in dip-slip motions[68], a sense of motion that is not favoured by the strike-slip stress regime in these regions[28]. Hence mining may not be as effective at releasing accumulated tectonic strain (as opposed to the strain accumulated by the induced deformation during coal mining), and this might therefore introduce a limit to maximum magnitudes during mining that does not exist for hydraulic fracturing.

The question of an appropriate M_{MAX}^P for HF in the UK remains relatively unconstrained. Comparisons between observed HF-IS in North America and values of M_{MAX}^P for tectonic seismicity suggest that the adoption of tectonic M_{MAX}^P values for HF-IS assessments would lead to a significant overestimation of the induced seismicity hazard. Hence, an appropriate value for M_{MAX}^P for hydraulic fracturing in the UK is almost certainly less than the tectonic values for the UK of M 6.5. However, it is probably larger than the M 3.0 estimated by Green et al.[30], since this level has almost been reached after the stimulation of only 3 wells. M_{MAX}^P is an important parameter and should be a focus for further research, and we are not able to provide further constraint within the scope of this study.

Hence, we do not adopt a value (or a distribution of possible values) for M_{MAX}^P here, and so it should be recognised that the recurrence rates estimated below simulate larger magnitude events (albeit at low probabilities of occurrence) that it may in fact not be physically possible to generate.

6.3. Workflow for probabilistic estimates of HF-IS occurrence

Event recurrence rates for probabilistic induced seismicity hazard assessments are typically based on prior observations of occurrence rates from analogous activities[29] – at what rate has stimulation of previous wells in the same formation generated induced seismicity of a given magnitude? The observed rate can be used to compute the likelihood that a new well generates induced seismicity, providing a probabilistic assessment of induced seismicity recurrence. However, this approach is not possible for formations in which little or no hydraulic fracturing has yet taken place, as there is insufficient data on which to base an empirical recurrence rate.

Instead, we develop a method for a priori probabilistic induced seismicity hazard assessment of formations in which little or no hydraulic fracturing has taken place. This approach is based on the seismogenic index[58], and the probabilistic quantification of earthquake rates and magnitudes that it provides. The seismogenic index, S_I, was derived by considering how a pore pressure pulse generated by injection would interact with pre-existing faults, or "seeds" that are randomly distributed within a reservoir[22,58]. In this scenario, S_I is given by:

$$S_I = \log_{10}\left(\frac{10^a F}{C.S}\right), \tag{5}$$

where a is the Gutenberg-Richter a value, F is the density of faults, C is the critical pore pressure increase required to reactivate the faults, and S is the storativity, which determines the size of pressure pulse – both its magnitude and the distance it propagates from the well – generated by the injection of a given volume.

The seismogenic index relates the number of induced events, N_E, larger than magnitude M, to the injected volume, V[58]:

$$S_I = \log_{10}\left(\frac{N_E}{V}\right) + bM, \tag{6}$$

where b is the Gutenberg-Richter b value. Eq. 6 can be re-written to

compute the expected number of earthquakes for a given injection volume in the case where S_I is known:

$$N_E = V.10^{S_I - bM}, \tag{7}$$

The S_I method has commonly been used to quantify and forecast the rate of occurrence of induced seismicity during subsurface operations[39, 64], and can be used to forecast the largest magnitude event expected during operations, M_{MAX}[58]:

$$M_{MAX} = \left(S_I - \log_{10}\left[\frac{-\ln\chi}{V}\right]\right)\bigg/ b, \tag{8}$$

where χ is the probability that a given magnitude is not exceeded.

In forecasting the expected induced seismicity hazard at a proposed hydraulic fracturing site using Eq. 8, the total injection volume is defined by the planned hydraulic fracturing schedule of the operator. The b value can reasonably be assumed to be 1.0[70], but S_I is unknown. Verdon[63] addressed this uncertainty by defining a range of potential S_I values with associated likelihoods, using Eq. 8 to calculate the probability of exceedance for all magnitudes, and then integrating these probabilities over all potential S_I values, weighted by the assigned probability of each S_I value.

In practice, constraining the geomechanical parameters that comprise Eq. 5 is not practicable during a priori site characterisation. As such, the seismogenic index is seldom calculated in this way[22]. Instead, S_I is typically measured from the observed scaling between earthquake rates and injection volumes during operations, with S_I values measured during the early phases of an operation being extrapolated forwards to make forecasts for later phases of activity[18,31,39,64].

While constraining a priori all of the terms in Eq. 5 may be challenging, the equation does provide a useful framework within which the effects of variations in key factors, such as stress conditions and/or faulting abundance, on the induced seismicity hazard can be quantified. Consider two theoretical sites, 1 and 2, and assume that at both sites the fault densities, F_1 and F_2, have been mapped using seismic imaging, while the seismogenic index at Site 1, S_{I1}, has been quantified through observations of seismicity rates during hydraulic fracturing. If it is assumed that C, S and a in Eq. 5 are the same, which might be reasonable in a play with relatively consistent lithological properties, then the seismogenic index at Site 2, S_{I2}, can be modelled as:

$$S_{I2} = S_{I1} - \log_{10}\left(\frac{F_1}{F_2}\right). \tag{9}$$

Put more simply, if the fault density at Site 2 is one order of magnitude smaller than at Site 1, then all other things being equal, the seismogenic index at Site 2 will decrease by 1.

Our approach is summarised in Fig. 14. We begin by constraining S_I values at an existing 'control' site where microseismic observations have been made, using the measured relationship between numbers of events and injection volumes (Eq. 6). For our application, we use the hydraulic fracturing in the PH and PNR wells[16,18,39]. In some cases, it may be more appropriate to characterise the observed seismicity with a distribution of S_I values or a logic tree, rather than a singular value.

We then quantify the differences in geomechanical conditions between the control site and potential sites at which future operations might be planned. In our case we have focussed on differences in fault density (with our results presented in Section 5). Differences in pore pressure gradient (which, as shown in Section 5.2, is usually the primary control on C) and storativity could be treated in an analogous manner, although we do not at present have sufficient data to do so for the Bowland Shale play. We use Eq. 9 to evaluate how the different geomechanical conditions between the control site and future sites will affect the seismogenic index, and thereby generate an updated S_I value (or distribution thereof) that can be applied to compute a priori the induced seismicity hazard for the proposed future sites.

If and when further operations are conducted, providing new
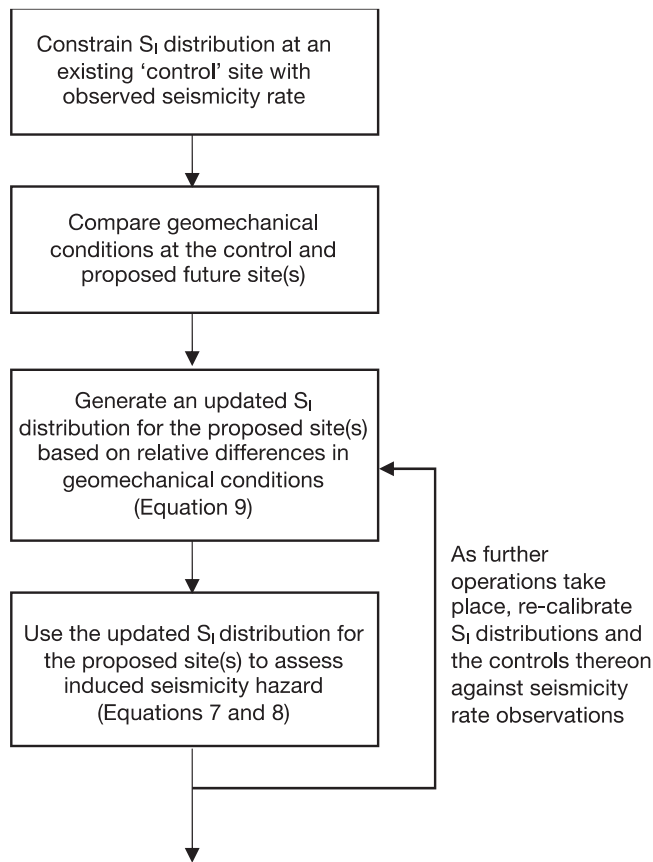
Fig. 14. Workflow for our seismic hazard assessment. We begin by defining a distribution of S_I values for a known site using observed induced seismicity rates. We then quantify the differences in geomechanical conditions (e.g., stresses and fault densities) between the existing site and proposed sites for future operations and use Eq. 9 to generate modelled S_I values with which we assess the a priori induced seismicity hazard at these future sites.

measurements of S_I from observed seismicity rates, we anticipate that the additional understanding of the geomechanical controls on S_I generated by these observations would allow for an iterative approach, incrementally improving the accuracy and precision of induced seismicity hazard estimates as the play is developed.

6.4. Application to the bowland shale play

To assess the potential consequences of the differences in fault density observed across the Bowland Shale play, we must first develop an appropriate range of S_I values for a control site – in this case the hydraulic fracturing at the PH and PNR wells. These values are constrained empirically from observed induced seismicity rates. Clarke et al.[18] and Kettlety et al.[39] observed S_I values ranging between $-3.5 < S_I < -0.5$. Since we have observed a range of values, we define a distribution for S_I with values spaced at intervals of 0.1 between values of $-5 \leq S_I \leq 1$, where the probability for each S_I value is defined by a normal distribution with a mean of -2 and a standard deviation of 0.66. The resulting distribution of S_I values is shown in Fig. 15a.

To check that this assumed distribution is appropriate for hydraulic fracturing on the Fylde Peninsula, we calculate the induced seismicity hazard that it produces. For each S_I value we use Eq. 8 to compute the distribution of M_{MAX} values, assuming a b value of 1.0 and an injection volume of 10,000 m^3 (which is typical for wells planned in the Bowland Shale to date). We weight each M_{MAX} probability curve by the likelihood of their respective S_I values, which produces the curves shown in Fig. 15b. We then integrate over all of these curves to compute the

overall M_{MAX} probability distribution (Fig. 15c), and the cumulative probability (Fig. 15d).

We compare these results with the actual induced events observed on the Fylde Peninsula in order to check their validity. The largest events were M_L 2.3 during stimulation of the PH well, M_L 1.5 during PNR-1z, and M_L 2.9 during PNR-2. Our estimated likelihoods for $M_{MAX} \leq 1.5$, 2.3 and 2.9 are 21%, 56%, and 80%. The most likely value for M_{MAX} is M 2.2, and the 5% and 95% confidence intervals for M_{MAX} are 0.8 and 3.6. Our estimated M_{MAX} likelihoods therefore do a good job of straddling the range of magnitudes that were actually observed during hydraulic fracturing of the PH and PNR wells.

Having established a reasonable distribution for S_I at our control site, we then adapt our distribution to evaluate how the observed differences in the densities of critically stressed faults moving eastwards across the play might affect the induced seismicity hazard. Our comparison of fault densities and stress conditions between the Fylde Bowland-12 survey and sites in the East Midlands indicated a reduction in the density of critically stressed faults by a factor of as much as 10. From Eq. 9 we see that a 10-fold reduction in fault density reduces S_I by 1. In Fig. 16a we generate a new distribution for S_I, where the mean value for S_I is set to -3 (i.e., reduced by a value of 1 from the control case). Fig. 16b shows the resulting cumulative probability distribution for M_{MAX} (calculated as per the steps in Fig. 15). The most likely value for M_{MAX} is M 1.2, and the 5% and 95% confidence intervals for M_{MAX} are -0.1 and 2.6. An earthquake of M 1.2 would almost certainly not be felt at the surface.

Note that these probabilities assume that no mitigating actions are taken by an operator during operations. Such actions might include following a TLS, or reducing injection volumes and skipping stages where evidence for incipient fault reactivation is identified. Note also that, as described above, these probabilities are derived from an unbounded Gutenberg-Richter distribution, whereas there may be geomechanical factors that limit the maximum magnitudes that can be generated by activities in these shallow (with respect to the hypocentres of most natural earthquakes) sedimentary strata.

7. Conclusion

From a theoretical perspective, the prevalence of HF-IS will be promoted by an increased abundance of pre-existing faulting and in situ stress conditions that are such that the faults area be close to the failure threshold (high pore pressures, high shear stresses). The prevalence of HF-IS will also be affected by the size of the subsurface perturbation generated, but it can be difficult to reduce this operationally since certain injection pressures and rates must be achieved during hydraulic fracturing in order to fracture the rock and carry proppant into the fractures. This perspective is supported by observed variations in the prevalence of HF-IS in North America.

Based on this understanding we examine the variability of these factors across the Bowland Shale. Existing fault maps and geological interpretations suggest a reduction in fault density along a west-east axis across northern England. We evaluate fault abundance across northern England within a compilation of six 3D reflection seismic surveys, using an automated method for fault identification to minimise any bias that could be introduced by manual fault interpretation. Having identified potential faults, we resolved estimated in situ stresses onto fault planes to evaluate critical pore pressures (the pore pressure increases required to generate slip).

We performed our analysis on lower Carboniferous strata, and we also examined middle Carboniferous formations that have been the subject of previous industrial operations (tight gas extraction from the Millstone Grits, coal bed methane from the Lower Coal Measures). We found that the absence of overpressure in the middle Carboniferous meant that faults were not critically stressed. This may explain why decades of hydraulic fracturing operations in the Millstone Grits have not generated any recorded cases of induced seismicity. The Bowland-12 survey on the Fylde peninsula had the highest intensity of faulting, with

(a)

(b)

(c)

(d)
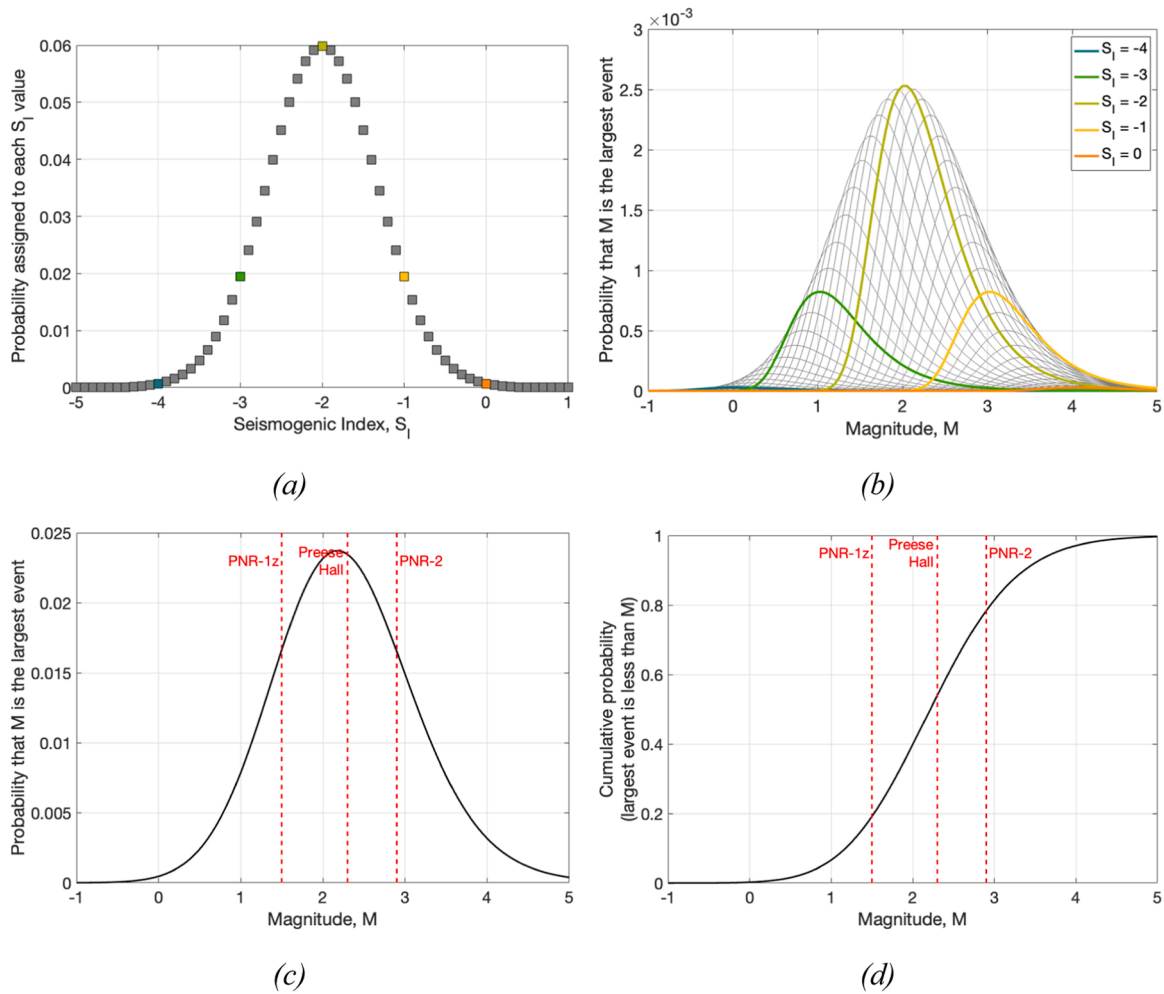
Fig. 15. Defining a distribution of S_I values for our control case – the induced seismicity observed at the PH and PNR wells. In (a) we show the distribution of probabilities assigned to potential S_I values; in (b) we show the M_{MAX} probability curves generated for each S_I value (weighted by the probability assigned to that S_I value). Each curve in (b) corresponds to an S_I value in (a). To show this, in (b) we have plotted the curves corresponding to S_I values of -4, -3, -2, -1, and 0 in colour, and have coloured the points in (a) accordingly. In (c) we integrate over the entire S_I distribution to compute the overall M_{MAX} probability, and in (d) we show the cumulative probability for M_{MAX}. In (c) and (d) we also show the largest events observed at the PH and PNR wells in order to compare the results of our assumed S_I distribution with what occurred at these sites.

(a)

(b)
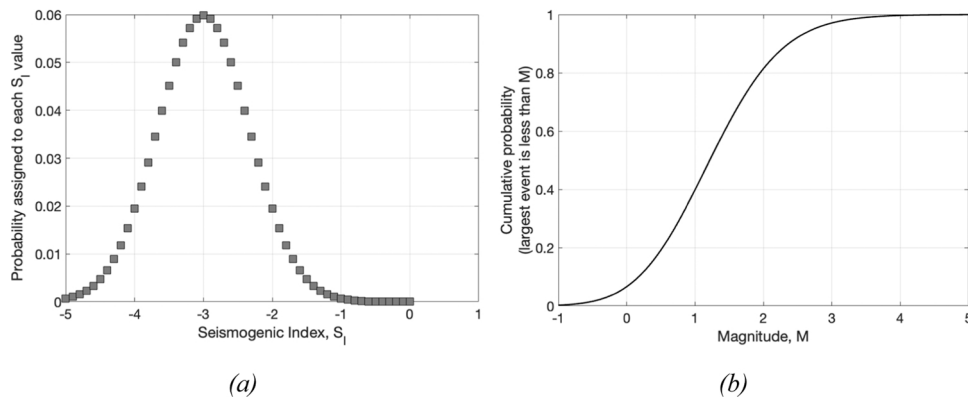
Fig. 16. Induced seismicity hazard assessment adapted to account for the lower density of faults across the eastern portion of the Bowland Play. The mean S_I value (shown in (a)) is decreased by 1 from the control case. In (b) we show the resulting cumulative probability for M_{MAX}.

fault intensities reducing in survey areas to the east by as much as an order of magnitude. The Bowland-12 survey is also the most consistently faulted across the entire survey area – while other surveys have large areas with no critically stressed faults, there are very few blocks in the

Bowland-12 area which do not contain critically stressed faults.

We use these observations to inform a probabilistic assessment of seismic hazard based on the seismogenic index model. Given the difficulties of constraining S_I a priori, we assign a distribution of values. We

begin by using the observed HF-IS in the Bowland-12 area as a control to create a baseline model that represents the observed seismicity generated at the PH and PNR wells. We then use the observed differences in fault densities to create an updated S_I distribution that is more appropriate for the less faulted regions to the east. This updated model shows that induced seismicity of sufficient magnitude to be felt could still be generated by hydraulic fracturing in these regions, however their likelihood of occurrence is reduced by an order of magnitude.

The largest source of uncertainty in our assessment is the absence of stress and pressure measurement data from within the Bowland Shale – measurements of these parameters from wells within regions of interest may enable more detailed and a more confident assessment of induced seismicity risk to be made.

CRediT authorship contribution statement

Rodríguez-Pradilla Germán: Data curation, Investigation, Validation, Visualization, Writing – original draft, Writing – review & editing. **Verdon James:** Conceptualization, Funding acquisition, Methodology, Writing – original draft, Writing – review & editing.

Declaration of Competing Interest

The BUMPS project is funded by a range of operating and oilfield service companies, some of whom hold interests in the development of shale gas in the UK. Some of the data used in this study was provided by Egdon Resources UK Ltd. and IGas Energy Plc., both of which hold interests in the development of both conventional and shale gas resources in the UK. In addition, JPV has acted as an independent consultant for a variety of organisations including hydrocarbon operating companies and governmental organisations on issues pertaining to induced seismicity. None of the aforementioned organisations had any input into the conception, development, analysis, or conclusions of this study.

Data Availability

Data was sourced from the UK Onshore Geophysical Library (https://ukogl.org.uk). The structural interpretations presented in this study were provided by operating companies and are not publicly available, with the exception of the BGS interpretation of the Bowland-12 survey[51]. The stress and pore pressure data are available from the World Stress Map dataset at https://datapub.gfz-potsdam.de/download/10.5880. WSM.2016.001/.

References

1. Anderson I, Underhill JR. Structural constraints on Lower Carboniferous shale gas exploration in the Craven Basin, NW England. *Pet Geosci.* 2020;26:303–324.
2. Andrews, I.J., 2013. The Carboniferous Bowland Shale gas study: geology and resource estimation. Department of Energy and Climate Change, London.
3. Aqrawi A, Boe T. Improved fault segmentation using a dip-guided and modified 3D Sobel filter: 81st SEG Annual Meeting. *Expand Abstr.* 2011:999–1003.
4. Armstrong, R., D. Daley, R. Lawley, A. Myers, A. Smith, 2016. User guide for the BGS Geology 50k dataset (V8): British Geological Survey Open Report, OR/16/46.
5. Atkinson GM, Ghofrani H, Assatourians K. Impact of induced seismicity on the evaluation of seismic hazard: some preliminary considerations. *Seismol Res Lett.* 2015;86:1009–1021.
6. Atkinson GM, Eaton DW, Ghofrani H, et al. Hydraulic fracturing and seismicity in the Western Canada Sedimentary Basin. *Seismol Res Lett.* 2016;87:631–647.
7. Bao X, Eaton DW. Fault activation by hydraulic fracturing in Western Canada. *Science.* 2016;354:1406–1409.
8. Beirlant, J., A. Kijko, T. Reynkens, J.H.J. Einmahl, 2017. Estimating the maximum possible earthquake magnitude using extreme value methodology: the Groningen case: arXiv:1709.07662.
9. Bishop I, Styles P, Allen M. Mining-induced seismicity in the Nottinghamshire coalfield. *Q J Eng Geol Hydrogeol.* 1993;26:253–279.
10. Bommer JJ. Earthquake hazard and risk analysis for natural and induced seismicity: towards objective assessments in the face of uncertainty. *Bull Earthq Eng.* 2022;20:2825–3069.
11. Bommer JJ, van Elk J. Comment on "The maximum possible and maximum expected earthquake magnitude for production-induced earthquakes at the gas field in Groningen, The Netherlands" by Gert Zöller and Matthias Holschneider. *Bull Seismol Soc Am.* 2017;107:1564–1567.
12. Bond CE, Lunn RJ, Shipton ZK, Lunn AD. What makes an expert effective at interpreting seismic images. *Geology.* 2012;40:75–78.
13. Bonnet E, Bour O, Odling NE, et al. Scaling of fracture systems in geological media. *Rev Geophys.* 2001;39:347–383.
14. Brudzinski MR, Kozłowska M. Seismicity induced by hydraulic fracturing and wastewater disposal in the Appalachian Basin, USA: a review. *Acta Geophys.* 2019;67:351–364.
15. Chopra S, Marfurt KJ. *Seismic attributes for prospect identification and reservoir characterisation.* Society of Exploration Geophysicists; 2007.
16. Clarke H, Eisner L, Styles P, Turner P. Felt seismicity associated with shale gas hydraulic fracturing: the first documented example in Europe. *Geophys Res Lett.* 2014;41:8308–8314.
17. Clarke H, Turner P, Bustin RM, Riley N, Besly B. Shale gas resources of the Bowland Basin, NW England: a holistic study. *Pet Geosci.* 2018;24:287–322.
18. Clarke H, Verdon JP, Kettlety T, Baird AF, Kendall J-M. Real time imaging, forecasting and management of human-induced seismicity at Preston New Road, Lancashire, England. *Seismol Res Lett 90, 1902-1915.* 2019.
19. Cowie PA, Scholz CH. Displacement-length scaling relationship for faults: data synthesis and discussion. *J Struct Geol.* 1992;14:1149–1156.
20. De Jonge-Anderson I, Ma J, Wu X, Stow D, Griffiths D. Bowland Shale well placement strategy – Part 2: Fracture simulations using a 3D geomechanical model and implications for stratigraphic and spatial horizontal well locations. *Energy Geosci.* 2022;3:235–254.
21. Dempsey D, Suckale J. Physics-based forecasting of induced seismicity at Groningen gas field, the Netherlands. *Geophys Res Lett.* 2017;44:7773–7782.
22. Dinske C, Shapiro SA. Seismotectonic state of reservoirs inferred from magnitude distributions of fluid-induced seismicity. *J Seismol.* 2013;17:13–25.
23. Eaton DW, Schultz R. Increased likelihood of induced seismicity in highly overpressured shale formations. *Geophys J Int.* 2018;214:751–757.
24. Eaton DW, Igonin N, Poulin A, et al. Induced seismicity characterization during hydraulic-fracture monitoring with a shallow-wellbore geophone array and broadband sensors. *Seismol Res Lett.* 2018;89:1641–1651.
25. Ester M, Kriegel HP, Sander J, Xu X. A density-based algorithm for discovering clusters in large spatial databases with noise. *Proc 2nd Int Conf Knowl Discov Data Min.* 1996:226–231.
26. Evensen D, Varley A, Whitmarsh L, et al. Effect of linguistic framing and information provision on attitudes towards induced seismicity and seismicity regulation. *Sci Rep.* 2022;12, 11239.
27. Eyre TS, Samsonov S, Feng W, Kao H, Eaton DW. InSAR data reveal that the largest hydraulic fracturing-induced earthquake in Canada, to date, is a slow-slip event. *Sci Rep.* 2022;12, 2043.
28. Fellgett MW, Kingdon A, Williams JDO, Gent CMA. Stress magnitudes across UK regions: new analysis and legacy data across potentially prospective unconventional resource areas. *Mar Pet Geol.* 2018;97:24–31.
29. Ghofrani H, Atkinson GM, Schultz R, Assatourians K. Short-term hindcasts of seismic hazard in the Western Canada Sedimentary Basin caused by induced and natural earthquakes. *Seismol Res Lett.* 2019;90:1420–1435.
30. Green, C.A., P. Styles, B.A. Baptie, 2012. Preese Hall shale gas fracturing review and recommendations for induced seismic mitigation: Department of Energy and Climate Change, London.
31. Hajati T, Langenbruch C, Shapiro SA. A statistical model for seismic hazard assessment of hydraulic-fracturing-induced seismicity. *Geophys Res Lett.* 2015;42:10601–10606.
32. Hale D. Methods to compute fault images, extract fault surfaces, and estimate fault throws from 3D seismic images. *Geophysics.* 2013;78:O33–O43.
33. Hansard. *House Commons Rep.* 2018;649(208):714–716.
34. Holmgren JM, Werner MJ. Raspberry Shake instruments provide initial ground-motion assessment of the induced seismicity at the United Downs deep geothermal power project in Cornwall, United Kingdon. *The Seismic Record.* 2021;1:27–34.
35. Igonin N, Verdon JP, Eaton DW. Seismic anisotropy reveals stress changes around a fault as it is activated by hydraulic fracturing. *Seismol Res Lett.* 2022;93:1737–1752.
36. Igonin N, Verdon JP, Kendall J-M, Eaton DW. Large-scale fracture systems are permeable pathways for fault activation during hydraulic fracturing. *J Geophys Res.* 2021;126, e2020JB020311.

37. Kettlety T, Verdon JP, Werner M, Kendall J-M. Stress transfer from opening hydraulic fractures controls the distribution of induced seismicity. *J Geophys Res.* 2020;125, e2019JB018794.

38. Kettlety T, Verdon JP, Werner MJ, Kendall J-M, Budge J. Investigating the role of elastostatic stress transfer during hydraulic fracturing-induced fault activation. *Geophys J Int 217, 1200-1216.* 2019.

39. Kettlety T, Verdon JP, Butcher A, Hampson M, Craddock L. High-resolution imaging of the M_L 2.9 August 2019 earthquake in Lancashire, United Kingdom, induced by hydraulic fracturing during Preston New Road PNR-2 operations. *Seismol Res Lett.* 2021;92:151–169.

40. Kim K-I, Yoo H, Park S, et al. *Int J Rock Mech Min Sci.* 2022;153, 105098.

41. Kingdon A, Fellgett MW, Williams JDO. Use of borehole imaging to improve understanding of the in-situ stress orientation of Central and Northern England and its implications for unconventional hydrocarbon resources. *Mar Pet Geol.* 2016;73: 1–20.

42. Li X, Main I, Jupe A. Induced seismicity at the UK "hot dry rock" test site for geothermal energy production. *Geophysical Journal International.* 2018;214: 331–344.

43. Mai PM, Thingbaijam KKS. SRCMOD: An online database of finite-fault rupture models. *Seismol Res Lett.* 2014;85:1348–1357.

44. Mancini S, Werner MJ, Segou M, Baptie B. Probabilistic forecasting of hydraulic fracturing-induced seismicity using an injection-rate driven ETAS model. *Seismol Res Lett.* 2021;92:3471–3481.

45. Marfurt K, Sudhaker V, Gersztenkorn A, Crawford K, Nissen S. Coherence calculations in the presence of structural dip. *Geophysics.* 1999;64:104–111.

46. McGarr A. Maximum magnitude earthquakes induced by fluid injection. *J Geophys Res.* 2014;119:1008–1019.

47. Mueller CS. The influence of maximum magnitude on seismic-hazard estimates in the central and eastern United States. *Bull Seismol Soc Am.* 2010;100:699–711.

48. Mustanen D, Fianu J, Pucknell J. Account of hydraulically fractured onshore wells in the UK and seismicity associated with these wells. *J Pet Sci Eng.* 2017;158:202–221.

49. Nantanoi S, Rodríguez-Pradilla G, Verdon JP. 3D-Seismic interpretation and fault slip potential analysis from hydraulic fracturing in the Bowland Shale, UK. *Pet Geosci.* 2022;28:2021–2057.

50. Park Y, Beroza GC, Ellsworth WL. Basement fault activation before larger earthquakes in Oklahoma and Kansas. *Seism Rec.* 2022;2:197–206.

51. Pawley S, Schultz R, Playter T, et al. The geological susceptibility of induced earthquakes in the Duvernay Play. *Geophys Res Lett.* 2018;45:1786–1793.

52. Pedersen S. *Image Feature Extr: U S Pat.* 2011;8, 055,026.

53. Randles T, Kingdon A, Smedley PL. Stratigraphic and structural interpretation of the released commercial "Bowland-12" 3D Seismic reflection survey data acquired in 2012. *Lancs Uk NERC EDS Natl Geosci Data Cent.* 2023. https://doi.org/10.5285/27c06acf-cf4f-4a1e-aafc-274f152a1fe5. last accessed 22/06/2023.

54. Reasenberg PA, Simpson RW. Response of regional seismicity to the static stress change produced by the Loma Prieta earthquake. *Science.* 1992;255:1687–1690.

55. Reyes-Canales M, Rodríguez-Pradilla G, Yusifbayov J, van der Baan M. The rise, peak and decline of the seismic hazard related to hydraulic fracturing activities in the Duvernay play, Fox Creek area, Alberta. *J Geophys Res.* 2022;127, e2021JB023060.

56. Rodríguez-Pradilla G, Eaton DW, Verdon JP. Basin-scale multi-decadal analysis of hydraulic fracturing and seismicity in western Canada shows non-recurrence of induced runaway fault rupture. *Sci Rep.* 2022;12, 14463.

57. Schultz R, Wang R. Newly emerging cases of hydraulic fracturing induced seismicity in the Duvernay East shale basin. *Tectonophysics.* 2020;779, 228393.

58. Shapiro SA, Dinske C, Langenbruch C, Wenzel F. Seismogenic index and magnitude probability of earthquakes induced during reservoir fluid stimulations. *Lead Edge.* 2010;29:304–308.

59. Skoumal RJ, Brudzinski MR, Currie BS. Proximity of Precambrian basement affects the likelihood of induced seismicity in the Appalachian, Illinois, and Williston Basins, central and eastern United States. *Geosphere.* 2018;14:1365–1379.

60. Van Bemmel, P. and R. Pepper, 2011. Seismic signal processing method and apparatus for generating a cube of variance values: U. S. Patent 6,151,555.

61. Van der Elst NJ, Page MT, Weiser DA, Goebel THW, Hosseini SM. Induced earthquake magnitudes are as large as (statistically) expected. *J Geophys Res.* 2016; 121:4575–4590.

62. Verdon JP. Significance for secure CO_2 storage of earthquakes induced by fluid injection. *Environ Res Lett.* 2014;9, 064022.

63. Verdon, J.P., 2020. Seismic hazard assessment for proposed proppant squeeze operation at the Wressle W-1 well: Hydraulic Fracture Plan for the Proppant Squeeze Operations Wressle-1 Well (W1), Egdon Resources U.K. Ltd.

64. Verdon JP, Budge J. Examining the capability of statistical models to mitigate induced seismicity during hydraulic fracturing of shale gas reservoirs. *Bull Seismol Soc Am.* 2018;108:690–701.

65. Verdon JP, Bommer JJ. Green, yellow, red, or out of the blue? an assessment of Traffic Light Schemes to mitigate the impact of hydraulic fracturing-induced seismicity. *J Seismol.* 2021;25:301–326.

66. Verdon JP, Rodríguez-Pradilla G. Assessing the variability in hydraulic fracturing-induced seismicity occurrence between North American shale plays. *Tectonophysics.* 2023;859, 229898.

67. Verdon JP, Kendall J-M, Horleston AC, Stork AL. Subsurface fluid injection and induced seismicity in southeast Saskatchewan. *Int J Greenh Gas Control.* 2016;54: 429–440.

68. Verdon JP, Kendall J-M, Butcher A, Luckett R, Baptie BJ. Seismicity induced by longwall coal mining at the Thoresby Colliery, Nottinghamshire, U.K. *Geophys J Int.* 2018;212:942–954.

69. Vilarrasa V, Carrera J. Geologic carbon storage is unlikely to trigger large earthquakes and reactivate faults through which CO_2 could leak. *Proc Natl Acad Sci.* 2015;112:5938–5943.

70. Watkins TJM, Verdon JP, Rodríguez-Pradilla G. The temporal evolution of induced seismicity sequences generated by long-term, low pressure fluid injection. *J Seismol.* 2023;27:243–259.

71. Westwood RF, Toon SM, Styles P, Cassidy NJ. Horizontal respect distance for hydraulic fracturing in the vicinity of existing faults in deep geological reservoirs: a review and modelling study. *Geomech Geophys Geo-Energy Geo-Resour.* 2017;3: 379–391.

72. Wilson MP, Worrall F, Davies RJ, Almond S. Fracking: how far from faults? *Geomech Geophys Geo-Energy Geo-Resour.* 2018;4:193–199.

73. Woessner J, Laurentiu D, Giardini D, et al. *2013 Eur Seism Hazard Model: key Compon Result: Bull Earthq Eng.* 2015;13:3553–3596.

74. Wozniakowska P, Eaton DW. Machine learning-based analysis of geological susceptibility to induced seismicity in the Montney Formation, Canada. *Geophys Res Lett.* 2020;47. e2020GL089651.

75. Zöller G, Holschneider M. The maximum possible and the maximum expected earthquake magnitude for production-induced earthquakes at the gas field in Groningen, the Netherlands. *Bull Seismol Soc Am.* 2016;106:2917–2921.